

1 **Title: Single-cell lineage trajectories and chromatin regulators that initialize antiviral CD8 T cell**
2 **ontogeny**

3

4 **Authors:** Huitian Diao^{1,2}, Runqiang Chen^{1,3†}, Shanel M. Tsuda^{1,2}, Dapeng Wang^{1†}, Megan A.
5 Frederick^{1†}, Jihye Kim¹, Pabalu P. Karunadharma⁴, Gustavo Martinez^{4†}, Adam J. Getzler^{1,2}, Clara
6 Toma⁵, Justin J. Milner^{5†}, Thomas C. Venables¹, Donna M. Martin⁶, Ananda W. Goldrath⁵, Shane Crotty³
7 and Matthew E. Pipkin^{1,2 *}

8 **Affiliations:**

9 ¹ Department of Immunology and Microbiology, The Scripps Research Institute, Jupiter, FL, USA

10 ² The Skaggs Graduate School of Chemical and Biological Sciences, The Scripps Research Institute,
11 Jupiter, FL, USA

12 ³ Division of Vaccine Discovery, La Jolla Institute for Immunology, La Jolla, CA.

13 ⁴ Genomics Core, The Scripps Research Institute, Jupiter, FL, USA

14 ⁵ Division of Biological Sciences, University of California, San Diego, La Jolla, California, USA.

15 ⁶ Department of Pediatrics, University of Michigan, Ann Arbor, MI, USA.

16 *Correspondence to: mpipkin@scripps.edu

17 †Additional author notes should be indicated with symbols (for example, for current addresses).

18 **Abstract:** Individual naive CD8 T cells activated in lymphoid organs differentiate into functionally
19 diverse and anatomically distributed T cell phylogenies in response to intracellular microbes. During
20 infections that resolve rapidly, including live viral vaccines¹, distinct effector (T_{EFF}) and memory (T_{MEM})
21 cell populations develop that ensure long term immunity². During chronic infections, responding cells
22 progressively become dysfunctional and “exhaust”³. A diverse taxonomy of T_{EFF}, T_{MEM} and exhausted
23 (T_{EX}) CD8 T cell populations is known, but the initial developmental basis of this phenotypic variation
24 remains unclear⁴⁻¹⁰. Here, we defined single-cell trajectories and identified chromatin regulators that
25 establish antiviral CD8 T cell heterogeneity using unsupervised analyses of single-cell RNA dynamics¹¹⁻¹³
26 and an *in vivo* RNAi screen¹⁴. Activated naive cells differentiate linearly into uncommitted effector-
27 memory progenitor (EMP) cells, which initially branch into an analogous manifold during either acute or
28 chronic infection. Disparate RNA velocities in single EMP cells initiate divergence into stem, circulating,
29 and tissue-resident memory lineages that generate diverse T_{MEM} and T_{EX} precursor states in specific
30 developmental orders. Interleukin-2 receptor (IL-2R) signals are essential for formation and
31 transcriptional heterogeneity of EMP cells, and promote trajectories toward T_{EFF} rather than T_{EX} states.
32 Nucleosome remodelers *Smarca4* and *Chd7* differentially promote transcription that delineates divergent
33 T_{MEM} lineages before cooperatively driving terminal T_{EFF} cell differentiation. Thus, the lineage
34 architecture is established by specific chromatin regulators that stabilize diverging transcription in
35 uncommitted progenitors.

36 **Main Text:**

37 To clarify the initial origins of T cell memory we generated longitudinal single-cell RNA-
38 sequencing (scRNA-seq) datasets and used unsupervised methods to map single-cell trajectories that
39 developed from naive CD8 T cells specific for *Lymphocytic choriomeningitis virus* (LCMV) early after
40 infection of wildtype mice with strains that cause either an acute (Armstrong, LCMV_{Arm}), or chronic
41 (Clone 13, LCMV_{Cl13}) infection (fig S1A-B) ¹⁵. On days 0 and 8 post infection (pi), clonal TCR transgenic
42 P14 cells that had been adoptively transferred and endogenous polyclonal MHC-I tetramer-reactive CD8
43 T cells (GP33⁺), which both recognize the LCMV epitope GP₃₃₋₄₁ in MHC H-2D^b, were isolated from the
44 spleens of the same host mice, and libraries were generated in parallel with fresh naive CD8 T cells
45 purified from separate P14 mice. Individual naive cells are recruited into the response over the first ~ 3
46 days following primary infection ¹⁶. Due to this asynchrony, we anticipated the time-series sampling
47 would encompass multiple developmental states that compose initial antiviral CD8 T cell ontogeny.

48 Dimensionality reduction and Louvain cluster extraction of cells was performed on all samples
49 simultaneously using similar numbers of randomly sampled cells from each experimental group to limit
50 potential biological biases arising from changes in subset compositions at different time points, and the
51 data are represented in the two-dimensional PAGA initialized force-directed (FA) embedding (Fig 1A

52 and fig S1B) ^{17,18}. Partition-based graph abstraction (PAGA) inferred single-cell paths based on
53 correlations between clusters ¹³, which were numbered according to pseudotime (P0-P10) to define a
54 potential developmental order (**Fig 1A-B**, Table S1). As expected, naive cells (P0) clustered apart from all
55 activated cells, which separated into multiple clusters (P1-P10) (**Fig 1A** and fig S1C-D) and the
56 pseudotime arrangement correctly predicted the actual time dependent emergence of cells in specific
57 clusters (naive, vs days 5 and 8 pi) (**Fig 1C**, S1C-D and Table S1). The distribution of P14 and GP33⁺
58 CD8 T cells among the clusters was similar in LCMV_{Arm}-infected mice (fig S1D and E). P14 cells
59 isolated from LCMV_{Arm} and LCMV_{Cl13} infected hosts were distributed in similar clusters on day 5 pi, but
60 contributed differentially to clusters on day 8 pi (**Fig 1C** and fig S2D and E). Cellular identities of the
61 clusters were imputed using gene set enrichment analysis (GSEA) and “subtractive” gene expression
62 signatures extracted from published bulk-RNA-seq data derived from phenotypically defined CD8 T cell
63 subsets ^{19,20} (Table S2, https://github.com/TCellResearchTeam/T_cell_signature_Reference). All major
64 T_{EFF}, T_{MEM}, T_{EX} and naive cell signatures were strongly enriched (p-val <0.05, NES) in at least one
65 Louvain cluster (**Fig 1D** and fig S1 J-M), and demonstrated that cells corresponding to all mature T_{EFF},
66 T_{MEM} and T_{EX} cell gene expression states arise within 8 days following acute or chronic LCMV infection.
67 The PAGA-inferred paths between these states facilitated precisely defining developmentally regulated
68 gene expression at the single-cell level, which extends previous longitudinal studies of bulk populations
69 during acute infection ²¹.

70

71 **Naive CD8 T cells differentiate along a linear path into common effector and memory progenitor
72 (EMP) cells**

73 The unsupervised approach clarified the initial developmental relationship of T_{MEM}, T_{EFF}, and T_{EX}
74 cells in an unbiased fashion (**Fig 1B**). Naive cells (P0) were connected to cells in cluster P2, via activated
75 intermediates (P1 cells, **Fig 1E** and Table S1). P2 cells were positively enriched with gene expression of
76 recent TCR stimulation (48h Act up, p = 0.004, NES = 2.1). P4 cells were negatively enriched with this
77 signature (fig S1K), and both GSEA and pseudotime indicated P4 cells were more developmentally
78 advanced than those in P2, and were therefore downstream (fig S1J, Best clusters 2, 8 and 10). Thus,
79 activated naive cells appeared to initially develop along a linear pathway into P2 cells.

80 Transcriptionally heterogeneous cell clusters on day 5 emerged from P2 cells, which strongly
81 expressed *Il2ra* (encodes CD25/IL-2Ra, a subunit of the trimeric interleukin-2 receptor that initiates high-
82 affinity IL-2 binding^{22,23}) and were positively enriched with signatures of both central memory (T_{CM}) and
83 naive cells, but not those of mature effector memory (T_{EM}), memory stem (T_{SCM}), resident memory (T_{RM})
84 or terminal effector (TE) cells (**Fig 1D** and fig S1L). P2 cells highly expressed a mixture of genes

85 encoding TFs whose cognate motifs are enriched within *cis*-acting regions that gain *de novo* chromatin
86 accessibility during primary TCR stimulation (*Runx3*, *Batf*, *Irf4*, *Prdm1*, *Klf2*), and that are essential for
87 both T_{EFF} and T_{MEM} cell development^{24,25} (fig S1G and H). In addition, genes encoding multiple regulatory
88 factors whose expression is highly differential in established mature TE/ T_{EM} (*Tbx21*, *Zeb2*, *Id2*, *Prdm1*),
89 T_{CM} / T_{SCM} / T_{EX}^{prog1} (*Tcf7*, *Zeb1*, *Bach2*, *Id3*), T_{RM} (*Hmmr*, *Aurkb*, *Prdm1*) and T_{EX}^{term} (*Tox*, *Lag3*, *Cd160*)
90 populations^{26,27} were coordinately expressed at intermediate levels in P2 cells (fig S1G and H). These
91 “lineage-specific” genes were significantly upregulated or downregulated in cells from clusters at the
92 distal tips of the paths (P10, P7, P3 and P8) compared to P2 cells (Fig 1E, fig S1G and H and Table S1),
93 implying P2 cells promiscuously express regulatory factors that become progressively lineage-restricted.
94 Flow cytometry confirmed that activated naive cells exhibited uniform behavior while undergoing
95 extensive cell division, upregulating CD25 and maintaining expression of T_{CM} cell attributes (CD27 and
96 *Tcf1* expression), before developing phenotypic features of more mature T_{EFF} cells (e.g., high Blimp1-
97 YFP and KLRG1 expression) (Fig 1F). These divergent subsets emerged near the final detectable cell
98 division from cells highly expressing both CD25 and the naive and T_{CM} -associated TF *Tcf1* (fig S1I).
99 Thus, naive cells initially differentiate in a linear path into cells that manifest multilineage gene
100 expression, a hallmark of multipotency and cells undergoing lineage-choice^{28,29}. On this basis, we
101 classified cells in cluster P2 as common effector/memory progenitor (EMP^{P2}) cells.

102
103 **Disparate RNA velocities develop in individual EMP cells and initiate a branched manifold that**
104 **establishes T_{MEM} and T_{EX} cell diversity**

105 Strong connections of EMP^{P2} cells with clusters arranged immediately downstream implied the
106 initial branchpoints of four developmental paths (Fig 1B). To define the trajectories of cells from each
107 cluster in the PAGA-inferred architecture, their future states were modeled using RNA velocity^{11,12} (Fig
108 2A). Nascent RNA expression precedes accumulation of their mature mRNAs by several hours, and RNA
109 velocity describes the rates at which cells are transitioning into new states based on the gene-wise ratios
110 in expression of nascent (i.e. unspliced) to mature (i.e., spliced) mRNAs genome-wide. Streamline plots
111 after UMAP embedding of all samples from each infection depicted transition probability data derived
112 from the grid average RNA velocities between single-cell clusters (Fig 2A and fig S2A), and defined
113 future cell states in the lineage architecture (Fig 2B and 2C fig S2A). Strongly divergent RNA velocities
114 in P2 and P5 cells confirmed they were developmental roots in each infectious context (fig S2B). The
115 RNA velocities of signature genes associated with multiple distinct CD8 T cell states (e.g., naive and
116 T_{SCM} cells: *Id3*, *Tcf7* and *Sell*; and TE cells: *Prdm1*, *Id2*, *Tbx21* and *Zeb2*) were all positive in EMP^{P2} cells
117 during LCMV_{Arm} infection (Fig 2E, Table S5). This indicates that multilineage gene transcription in

118 rapidly dividing $\text{EMP}^{\text{P}2}$ cells establishes the transition potential into diverse future cell states, prior to
119 developmental branching and mature lineage-specific mRNA expression. Conversely, cells in cluster P10
120 during LCMV_{Arm} infection, and clusters P7 and P8 during $\text{LCMV}_{\text{Cl13}}$ infection, lacked RNA velocities
121 into other clusters indicating they were terminal states in the analysis (fig S2C).

122 Trajectory 1 (T1: $\text{P2} \rightarrow \text{P4} \rightarrow \text{P9} \rightarrow \text{P10}$) only formed in LCMV_{Arm} -infected mice and defined
123 formation of cells enriched with signatures of bulk T_{EM} cells (effector memory precursors, $\text{pT}_{\text{EM}}^{\text{P}4}$),
124 classical KLRG1^{lo} CD127^{lo} early effector cells (EE $^{\text{P}9}$) and KLRG1^{hi} CD127^{lo} terminal effector (TE) cells
125 ($\text{TE}^{\text{P}10}$) (**Fig 2C-D**, fig S1K and M). RNA velocity-derived transition probabilities indicated most EE $^{\text{P}9}$
126 cells proceed toward $\text{TE}^{\text{P}10}$ cells (**Fig 2B**). Positive Tbx21 RNA velocity was sustained and Zeb2 velocity
127 accelerated in EE $^{\text{P}9}$ cells, followed by increased expression of mature Tbx21 and Zeb2 mRNAs in $\text{TE}^{\text{P}10}$
128 cells, whose velocities continued to increase in $\text{TE}^{\text{P}10}$ cells³⁰⁻³² (**Figs 2D-E** and fig S2D and Table S5).
129 Thus, the initial developmental order of T_{CIRC} cells during acute LCMV infection is T_{CM} to T_{EM} to TE
130 cells.

131 Trajectory 2 (T2: $\text{P2} \rightarrow \text{P5} \rightarrow \text{P3}$) is likely a main source of T_{RM} precursor cells ($\text{pT}_{\text{RM}}^{\text{P}3}$) during
132 LCMV_{Arm} infection, and exhausted progenitor 2 ($\text{T}_{\text{EX}}^{\text{prog2-P}3}$) cells³³ during $\text{LCMV}_{\text{Cl13}}$ infection. In
133 LCMV_{Arm} -infected hosts, P5 cells were positively enriched with signatures of bulk $\text{KLRG1}^{\text{hi}}\text{CD127}^{\text{hi}}$
134 “double positive” (DP) effector and T_{RM} cells, and were classified as DP $^{\text{P}5}$ cells (**Fig 1D** and fig S1K).
135 DP $^{\text{P}5}$ cells diverged into $\text{pT}_{\text{RM}}^{\text{P}3}$ cells, $\text{pT}_{\text{EM}}^{\text{P}4}$ cells, and cells enriched with the bulk signature of classical
136 $\text{KLRG1}^{\text{lo}}\text{CD127}^{\text{hi}}$ memory precursor (MP) cells (MP $^{\text{P}6}$) (**Figs 1B and 2A-C** and fig S1K-L). Runx3-
137 dependent gene expression was positively enriched in DP $^{\text{P}5}$ and MP $^{\text{P}6}$ (fig S1K and S2F), consistent with
138 the requirement of Runx3 for development of these cell states^{25,34}, and divergence into $\text{pT}_{\text{RM}}^{\text{P}3}$ cells
139 correlated with increased expression of the representative T_{RM} signature gene *Hmmr* (**Fig 2B-D**, and fig
140 S1H). In $\text{LCMV}_{\text{Cl13}}$ -infected hosts P5 cells were also enriched with signatures of DP and T_{RM} cells,
141 however, they were classified as $\text{T}_{\text{EX}}^{\text{prog2-P}5}$ cells because they were positively enriched with the signatures
142 of both $\text{T}_{\text{EX}}^{\text{prog2}}$ and T_{EX} cells (**Fig 1D** and fig S1L-M). In addition, cluster P3 cells were enriched with
143 both T_{RM} and $\text{T}_{\text{EX}}^{\text{prog2}}$ signatures, and were classified as $\text{T}_{\text{EX}}^{\text{prog2-P}3}$ cells, but were distinct from $\text{T}_{\text{EX}}^{\text{prog2-P}5}$
144 cells because they lacked TCR-stimulated gene expression (fig S1K-L). The T_{EX} signature was not
145 strongly enriched in either DP $^{\text{P}5}$ or $\text{pT}_{\text{RM}}^{\text{P}3}$ cells from LCMV_{Arm} -infected mice, which confirmed their
146 distinction from homologous cells during chronic infection which were and that strongly expressed *Tox*³⁵⁻
147 ³⁷ (**Figs 1D and 2E**, and fig S1M).

148 Trajectory 3 (T3: $\text{P2} \rightarrow \text{P6} \rightarrow \text{P8}$) explained initial development of intermediately exhausted ($\text{T}_{\text{EX}}^{\text{int}}$)
149 and terminally exhausted cells ($\text{T}_{\text{EX}}^{\text{term}}$) during $\text{LCMV}_{\text{Cl13}}$ infection, and formation of classical MP cells
150 during LCMV_{Arm} infection (**Fig 2C**). In LCMV_{Arm} -infected hosts, MP $^{\text{P}6}$ cells were enriched with MP and

151 EE cell signatures and had transition potential into EE^{P9} cells, providing an alternative conduit into the T1
152 trajectory (**Fig 2A-C**, fig S1K-M), and demonstrated classical MP cells are most likely distinct from
153 precursors of T_{SCM} (see below). P6 cells from LCMV_{Cl13}-infected were classified as T_{EX}^{int-P6} cells because
154 they manifested signatures of both intermediately exhausted (T_{EX}^{int}) and T_{EX} cells, and flowed directly
155 into cluster P8 cells (**Fig 2A-D**), which were designated T_{EX}^{term-P8} cells because they were strongly
156 enriched with the T_{EX}^{term} cell signature (**Fig 1D**, fig S1M) and highly expressed *Tox*, *Pdcd1* and *Lag3* (**Fig**
157 **1E and G**). Thus, T_{EX}^{int} cells are related to classical MP cells, but exhibit altered transition probabilities
158 into terminal states and fail to establish the T_{CIRC} lineage during LCMV_{Cl13} infection (**Fig 2B-D** and fig
159 S2C).

160 Trajectory 4 (T4: P2> P7) defined formation of precursors of T_{SCM}-like cells during acute
161 (T_{SCM}^{P7}) or chronic (T_{EX}^{prog1-P7}) LCMV infection (**Fig 2C**). T_{SCM}^{P7} cells from LCMV_{Arm}- infected hosts
162 were positively enriched with T_{SCM} and T_{CM} cell signatures, and were strongly connected to pT_{EM}^{P4} and
163 EE^{P9} cells (**Fig 1D** and fig S1J-K). Both T_{SCM}^{P7} and pT_{EM}^{P4} cells exhibited strong *Tbx21* RNA velocity,
164 suggesting they both manifest transition potential into *Tbx21* expressing states. Consistent with this, cells
165 in both clusters exhibited strong transition probabilities into EE^{P9} cells, indicating that T_{SCM} precursors
166 during LCMV_{Arm} infection are poised with T_{EFF} cell potential. In contrast, although T_{EX}^{prog1-P7} cells from
167 LCMV_{Cl13}-infected hosts were positively enriched with the T_{SCM} signature, they exhibited reduced *Tbx21*
168 RNA velocity (Table S5), and lacked transition probability into EE^{P9} cells (**Fig 2B**). In addition, T_{EX}^{prog1-P7}
169 cells appeared to derive from EMP^{P2-Cl13} cells initially, but their strong accumulation by day 8 pi
170 correlated with retrograde transition potentials from all downstream T_{EX} cell clusters except T_{EX}^{prog2-P3}
171 cells, whereas during LCMV_{Arm} infection, T_{SCM}^{P7} cells derived predominantly from EMP^{P2} cells (**Fig 2B-D**).
172 Moreover, T_{EX}^{prog1-P7} cells more strongly induced *Tcf7* (**Fig 2D**), highly expressed *Lag3*, *Pdcd1*, *Tox*,
173 *Tox2* and *Bcl6*, were positively enriched with the specific T_{EX} cell signature and were enriched with
174 terminal states (**Fig 1D** and figs S1H, M and S2C). Thus, the precursors of T_{SCM} cell states during acute
175 and chronic infections have different origins and distinct developmental potentials.

176 **IL-2R-dependent transcription establishes EMP cells and transcriptional heterogeneity**

177 The most dynamic genes drive the RNA velocity vector field ^{11,12}. Those encoding TFs, CRFs,
178 and surface receptors (SRs) during transitions between clusters were identified as potential drivers that
179 compose the antiviral CD8 T cell architecture (**Fig 2C** and fig S2D-E, Table S4). Strong *Il2ra* dynamics
180 and its transiently high expression in EMP^{P2} cells indicated IL-2R-dependent signals might promote
181 multilineage potential (**Fig 3A and B**). To define the role of *Il2ra* functionally, single cell trajectories
182 were inferred after scRNA-seq analysis of wildtype and *Il2ra*-deficient P14 (P14 *Il2ra*^{-/-}) CD8 T cells 6
183 days after LCMV_{Arm} infection (**Fig 3C and D**, as described fig S1B). This second analysis confirmed the

184 original lineage architecture during LCMV_{Arm} infection (**Fig 3C** and refer to **Fig 1A**). Louvain clusters
185 from the *Il2ra* analysis (designated “Exp-*Il2ra*”) closely matched most clusters identified on days 5 and 8
186 pi in the original analyses (**Fig 3D** and refer to **Fig 1**). PAGA-inferred connectivity and RNA velocities
187 implied analogous intracluster transition probabilities (**Fig 3C and E**), and analogous single cell behavior
188 of wildtype P14 cells in both the original and Exp-*Il2ra* analyses emphasized that the inferred lineage
189 architecture is biologically robust.

190 P14 *Il2ra*^{-/-} CD8 T cells distributed within the trajectories aberrantly compared to WT P14 cells.
191 P14 *Il2ra*^{-/-} cells almost entirely composed cluster Exp-*Il2ra*^{P1} compared to wildtype P14 cells indicating
192 they arrested before transition into EMP^{P2} cells (Exp-*Il2ra*^{P2}) (**Fig 3F** and fig S3E, p-value 1.35 x 10⁻²⁷).
193 Exp-*Il2ra*^{P1} cells were activated (data not shown), but lacked RNA velocity into future states indicating
194 they were terminal (fig S3D). Strong differential expression between Exp-*Il2ra*^{P1} and Exp-*Il2ra*^{P2} cells
195 confirmed *Il2ra* was essential for transition into EMP^{P2} cells (**Fig 3I**). In addition, differential expression
196 between wildtype and *Il2ra*^{-/-} P14 cells in cluster Exp-*Il2ra*^{P2} confirmed IL-2 signaling was required for
197 EMP cell formation (fig S3G). This required IL-2R-dependent transcription, because genes whose nascent
198 RNA expression required *Il2ra* for upregulation after TCR stimulation (WT^{48h} > WT^{naive}, padj < 0.05)
199 were positively enriched with those upregulated as Exp-*Il2ra*^{P1} transitioned into Exp-*Il2ra*^{P2} cells (fig
200 S3K, NES = 1.26, pvalue = 0.04), whereas genes that required *Il2ra* for downregulation (WT^{48h} > *Il2ra*^{-/-}
201 .^{48h}, padj < 0.05) were positively enriched with those downregulated in this transition (fig S3K, NES = -
202 1.16, pvalue = 0.05). Thus, IL-2R-dependent transcription *in vivo* is essential for gene expression that
203 drives activated naive cells to become EMP^{P2} cells.

204 Development beyond the EMP^{P2} cell state also required IL-2R signals. The transition
205 probabilities of P14 *Il2ra*^{-/-} cells into other clusters were substantially altered (**Fig 3E**). *Il2ra*^{-/-} cells in
206 cluster Exp-*Il2ra*^{P2} lacked transition potential (**Fig 3E**). Those from cluster Exp-*Il2ra*^{P4} did not manifest
207 velocity into Exp-*Il2ra*^{P5} (T_{RM}) cells, and those in Exp-*Il2ra*^{P5} were vectored backward into cluster Exp-
208 *Il2ra*^{P2} (**Fig 3E**). Consistent with this, P14 *Il2ra*^{-/-} cells were depleted from cluster Exp-*Il2ra*^{P5} cells
209 (pT_{RM}^{P3} analog) (**Fig 3F** and fig S3E, p-value 0.057), and those that did accumulate in that cluster were
210 negatively enriched with the T_{RM}-signature compared to wildtype P14 Exp-*Il2ra*^{P5} cells (fig S3F). Thus,
211 *Il2ra*^{-/-} P14 cells that bypassed the initial developmental block inefficiently formed putative T_{RM}
212 precursors. In addition, *Il2ra*^{-/-} cells in cluster Exp-*Il2ra*^{P4} manifested retrograde vectors into Exp-*Il2ra*^{P3}
213 (T_{SCM}) cells, unlike wildtype P14 cells (**Fig 3E**), which correlated with increased P14 *Il2ra*^{-/-} cell
214 representation in cluster Exp-*Il2ra*^{P3} (T_{SCM}^{P7} analogs) (**Fig 3F** and fig S3E, p-value 0.00042). Furthermore,
215 *Il2ra*-deficient cells inefficiently repressed T_{SCM} signature genes after TCR stimulation (fig S3J). These

216 results demonstrate that IL-2R signals promote divergent transcription in EMP cells that establishes
217 trajectories into branching T_{MEM} cell lineages.

218 The bias of EMP-like *Il2ra*^{-/-} cells toward T_{SCM}-like states and their reduced contribution to other
219 T_{MEM} precursor states during acute infection prompted examining IL-2R-regulated genes in EMP^{P2} cells
220 from LCMV_{Cl13}-infected mice. EMP^{P2} cells during LCMV_{Cl13} infection less highly expressed IL-2R-Stat5
221 induced genes (*Batf3*, *Ccr5*, *Gzmb*, *Chd7* see below) that promote formation of protective T_{EFF} and T_{MEM}
222 cells (fig. S3L). The IL-2R-repressed gene signature was enriched with genes whose RNA velocity was
223 greater in EMP^{P2} cells from LCMV_{Cl13}-infected mice (fig S3M). Moreover, in LCMV_{Cl13} infection,
224 T_{EX}^{prog1-P7} cells upregulated the IL-2R-repressed gene signature compared to EMP^{P2} cells; whereas this
225 signature was not upregulated as EMP^{P2} transitioned to T_{SCM}^{P7} cells during LCMV_{Arm} infection (fig S3M).
226 Thus, regulation of IL-2R-dependent genes appear to bias the future states of EMP^{P2} cells during acute
227 and chronic infection.

228

229 **Differential utilization of CRFs establishes antiviral CD8 T cell heterogeneity**

230 Chromatin structure in naive cells is remodeled during initial TCR and IL-2 stimulation and
231 becomes stably differential in distinct T_{EFF}, T_{MEM} and T_{EX} cell subsets³⁸. To identify chromatin regulatory
232 factors (CRFs) that might control diverging transcriptional programs during T_{EFF} and T_{MEM} cell formation
233 we screened a library of retrovirally delivered microRNA-embeded short hairpin RNAs (shRNAmirs)
234 targeting nearly all murine CRF genes using a pooled approach in P14 CD8 T cells responding to
235 LCMV_{Arm} infection (fig S4A and B, **Fig 5A** and Table S7)¹⁴. Candidate CRFs were identified by
236 sequencing DNA libraries amplified from integrated shRNAmir proviral sequences in FACS-purified
237 CD8 T cell subsets and quantifying differential shRNAmir representation (RNAi-induced effects) (**fig**
238 **S4B**, <https://github.com/Yolanda-HT/HSAP>). Genes with top RNAi-effects (25th percentiles) affecting *in*
239 *vivo* P14 cell accumulation (input vs output), maturation of KLRG1^{lo} CD127^{lo} cells into all other
240 phenotypes (EE vs other), and the balance between TE and MP cells (KLRG1^{hi}CD127^{lo} vs
241 KLRG1^{lo}CD127^{hi}) were selected as potential candidates (**Fig 4B-E** and Table S7). Individual follow-up
242 experiments confirmed specific phenotypes of several top candidates that were previously unknown,
243 including *Prmt5*, *Carm1*, *Taf1*, *Mll1* (manuscript in preparation) and multiple genes encoding factors in
244 Brg1-associated factor (BAF, mammalian SWI/SNF)³⁹ and chromodomian helicase and DNA-binding
245 (Chd) nucleosome remodeling complexes (**Fig 4B-D**). Thus, concerted activity of many CRFs

246 differentially control formation of classically defined populations defined by KLRG1 and CD127
247 expression during acute viral infection.

248 We pursued *Smarca4* (Brg1) and *Chd7* (Chd7), which encode ATPases of nucleosome
249 remodeling complexes that have essential roles in multipotent neural crest cells⁴⁰, human development
250 and immune system function⁴¹⁻⁴³, and thymic T cell development⁴⁴. Their strong phenotype in the screen
251 and their dynamics in the single-cell trajectory, both implied they could have essential functions in EMP
252 cells. Depletion of either factor alone impaired formation of KLRG1^{hi} cells on day 5 pi, and increased the
253 fractions of KLRG1^{lo} CD127^{lo} EE-like cells by day 8 pi, which suggested both factors might promote
254 divergence into TE, DP or MP populations⁴ (**Fig 5B**). In addition, RNAi-effects in the primary screen
255 indicated *Smarca4* and at least 4 additional BAF subunits (*Arid1a*, *Smarcc1*, *Smarce1*) were selectively
256 required for TE cell formation (**Fig 4C**). Four other BAF-subunits (*Actl6b*, *Smarcc2*, *Smarcd1*, and
257 *Smarcd3*) were preferentially required for MP formation (**Fig 4C**). Thus, distinct BAF-complex
258 assemblies might differentially bias TE and MP cell development³⁹. To further confirm the role of Chd7,
259 engineered *Chd7* alleles⁴² were conditionally disrupted in mice using transgenic Cre expression in post-
260 thymic T cells (referred to as *Chd7*^{f/f} dLck-Cre sfYFP). Similar to RNAi, *Chd7* gene-disruption impaired
261 the frequency of KLRG1^{hi} cells 5 days after LCMV_{Arm} infection (fig S4C), and reduced formation of TE
262 cells while increasing frequencies of EE- and MP-like cells 8 days after infection, without strongly
263 affecting overall T_{EFF} cell numbers (**Fig 4E**). Thus, both BAF and Chd7 complexes are essential for the
264 early phenotypic heterogeneity of T_{EFF} cells during acute infection.

265

266 **Smarca4 and Chd7 are required for transcriptional heterogeneity of EMP cells**

267 Distinct RNA dynamics of *Smarca4* and *Chd7* in the trajectory implied sequential early functions
268 during initial lineage divergence. Mature *Smarca4* mRNA expression was greatest in EMP^{P2} cells, before
269 *Chd7* RNA velocity increased in EMP^{P2}, DP^{P5} and MP^{P6} cells (**Fig 4G**). Mature *Chd7* transcripts were
270 upregulated in EE^{P9} and TE^{P10} cells (**Fig 4G**) and in bulk KLRG1^{hi} cells on day 5 of LCMV_{Arm} infection²⁵.
271 *Chd7* transcription required *Il2ra* during TCR stimulation (**Fig 3K**). These data are consistent with
272 *Smarca4* and *Chd7* functioning in an IL-2R-dependent transcriptional network. To examine this
273 possibility, P14 cells depleted of either *Smarca4* or *Chd7* were analyzed by RNA-seq 5 days after
274 LCMV_{Arm} infection. *Smarca4* was required to downregulate genes that are repressed by IL-2R (day 6),
275 and to repress both the T_{SCM} and *Tcf7*-promoted gene expression signatures^{21,25,36,45-47} (**Fig 4H**), whereas
276 *Chd7* was required for activation of genes that require IL-2R for expression at later times (day 10)⁴⁶ (**Fig**
277 **4H**). In addition, both factors were necessary for promoting gene expression activated by the TF Runx3
278 and repressing gene expression promoted by the TF Tox (**Fig 4H**). Thus, IL-2R-dependent transcriptional

279 heterogeneity that develops in EMP cells early during acute infection required both Smarca4 and Chd7. In
280 addition, the distinct requirements of each factor indicated they differentially promote transcription that
281 drives divergence between T1 (pT_{EM}), T2 (MP) and T4 (pT_{SCM}) trajectories.

282 Smarca4 and Chd7 stabilized transcription that drives formation of the T1 trajectory. *Smarca4*-
283 depleted P14 cells on day 5 pi expressed significantly less *Bhlhe40*, *Chd7*, *Gzma*, *Med12l*, *Runx3*, *Tbx21*
284 and *Zeb2* (**Fig 4I, left**); *Chd7*-depleted cells expressed significantly less *Gzma*, *Il12rb2*, *Il18rap*, *Med12l*
285 and *Zeb2*, while expression of *Bhlhe40*, *Batf3*, and *Tbx21* trended lower (**Fig 4I, right**). In P14 cells
286 depleted of Chd7, T-bet protein expression and TE cell formation was more strongly impaired during
287 LM_{GP33} infection than during LCMV_{Arm} infection, consistent with grossly impaired *Il12rb2* expression
288 (**Fig 4I, right**), and the increased IL-12 concentrations during LM infection compared to LCMV
289 infection^{30,48} (**Fig 6J-K** and data not shown). Complementation of Smarca4 or Chd7 depleted P14 cells
290 with retrovirally expressed Tbx21 restored the normal pattern of TE and MP in each case (fig 4D and E),
291 indicating they each promote T_{EM} and TE differentiation by ensuring *Tbx21* expression. However,
292 enforced T-bet expression in the absence of *Chd7* did not rescue defective Gzmb expression, indicating
293 that Chd7 is broadly required for cytolytic effector cell programming (data not shown). Because altered
294 gene expression in the absence of Smarca4 and Chd7 is manifest on day 5 pi, prior to EE^{P9} cell formation,
295 these results demonstrate that both CRFs are necessary to establish T_{EFF} gene expression prior to when
296 cells with these phenotypes manifest.

297

298 Chd7 is essential for T_{MEM} cell lineage branching

299 P14 cells depleted of Chd7 during LCMV_{Arm} infection were positively enriched with gene
300 expression signatures of DP^{P5} and MP^{P6} cells on day 5 pi, which correlated with increased frequencies of
301 EE and MP-phenotype cells in *Chd7*^{fl/fl} dLck-Cre sfYFP mice 8 days after LCMV_{Arm} infection (**Fig 4F**).
302 Thus, cells lacking Chd7 appeared to arrest at the point where EMP^{P2} cells undergo branching into MP^{P6}
303 and EE^{P9} cells, well before maturation of TE^{P10} cells, which brought into question whether they correctly
304 stabilized the specific gene expression programs related to each of these flow cytometry phenotypes. To
305 examine this directly, LCMV-specific CD8 T cells from *Chd7*^{+/+} and *Chd7*^{fl/fl} dLck-Cre⁺ sfYFP⁺ mice that
306 exhibited MP, EE, DP and TE cell phenotypes 8 days after LCMV_{Arm} infection were FACS-purified and
307 analyzed using RNA-seq. Multidimensional scaling showed these populations from wildtype mice were
308 separated from each other, whereas those from *Chd7*-deficient mice grouped (**Fig 4L**), indicating that
309 gene expression states which diverged in wildtype T_{EFF} subsets did not strongly diverge in the *Chd7*-
310 deficient populations. Consistent with this interpretation, pairwise analysis showed that compared to
311 wildtype cells, *Chd7*-deficient TE-phenotypic cells less strongly expressed genes encoding factors

312 characteristic of TE cells (*Zeb2*, *Med12l*, *Il18rap*, *Il12rb2*), and *Chd7*-deficient EE- or MP-phenotypic
313 cells less highly expressed genes that promote MP cell development and formation of long-lived T_{MEM}
314 cells (*Tcf7*, *Id3*, *Tox*, and *Ccr7*) (Fig 4M). These results demonstrate that *Chd7* is necessary to stabilize
315 divergent transcriptional programs that differentiates circulating T_{MEM} lineage branches and maturing cell
316 states, and promotes terminal T_{EFF} maturation.

317

318 **Discussion**

319 Our study resolves the initial stages of antiviral CD8 T cell ontogenesis. The architecture
320 indicates naive cells differentiate into common EMP cells which diverge along distinct trajectories that
321 develop gene expression states within the first week of acute or chronic viral infection that match all
322 major T_{EFF}, T_{MEM} and T_{EX} cell populations found at later times. Additional developmental paths to cells
323 that were not sampled in this analysis could exist (e.g., cells from other tissues)^{49,50}. Variable RNA
324 velocities that develop in EMP cells indicates that diverging transcription initiates the branching
325 trajectories before strong differential expression of lineage-specific regulators is established. IL-2R
326 signals were required for EMP cell development and their transcriptional heterogeneity, and altered IL-
327 2R-dependent transcription in EMP cells during chronic infection correlated with development of T_{EX} cell
328 states. Because *Il2ra* is regulated by IL-2 stimulation and was dynamic during EMP cell formation and
329 divergence, these results suggest variable IL-2 stimulation contributes to initial lineage bias of cells in the
330 population.

331 We provide evidence that diverse T_{MEM} cell types most likely arise from divergent precursor cell
332 states derived from distinct lineages early in the response. The nucleosome remodeler Smarca4 was
333 necessary for gene expression that initially separates T_{SCM} and T_{EM} precursor states; Chd7 functioned later
334 to mature classical MP cells; and, both factors cooperatively promoted TE cell differentiation. These
335 results provide evidence that diverging transcriptional states in EMP cells are stabilized by specific CRFs,
336 and implies that chromatin remodeling reinforces initial lineage biases and establishes the branching
337 architecture. Thus, differential chromatin remodeling in divergent T_{MEM} cell precursor lineages might
338 explain the preferential interconversion potentials of distinct mature T_{MEM} cell populations^{1,51,52}, and
339 resistance of T_{EX} cells to chromatin-level reprogramming^{53,54}. The developmental architecture, stepwise
340 transcriptional dynamics and CRF atlas described here suggests many factors with spatiotemporally
341 resolved functions and might suggest strategies for engineering T_{MEM} CD8 T cell formation.

342 **Methods**

343 **Mice**

344 Wildtype 6-8 week old C57BL/6J mice were used as recipients for adoptive transfer experiments
345 and were purchased from the Jackson Laboratory. P14 Thy1.1⁺ mice were a gift from Dr. Rafi Ahmed
346 (Emory University). P14 Thy1.1⁺ Thy1.2⁺ mice were generated by crossing P14 Thy1.1⁺ mice with
347 wildtype C57BL/6J mice. P14 Thy1.1⁺ *Il2ra*^{-/-} mice were generated by crossing *Il2ra*^{-/-} mice (purchased
348 from Jackson Laboratory) with P14 Thy1.1⁺ mice. *Chd7*^{fl/fl} mice were a gift from Dr. Donna M. Martin
349 (University of Michigan)⁴², and were crossed with Rosa26-EYFP and dLck-Cre (maintained
350 heterozygous) transgenic mice. All mice were maintained in specific-pathogen free facilities and used
351 according to protocols approved by the Institutional Animal Care and Use Committee of TSRI-FL.

352

353 **T cell activation, adoptive transfer and infections**

354 Naive P14 CD8⁺ T cells from wildtype mice were isolated by negative selection (EasySepTM,
355 Stemcell Technologies). Naive P14 Thy1.1⁺ *Il2ra*^{-/-} cells were isolated from 4-5 week old mice by
356 depleting CD44^{hi} cells (Biolegend biotin anti-mouse/human CD44, clone IM7, 2µl per spleen). For *Il2ra*^{-/-}
357 single cell experiment, cells were further sorted for CD44^{lo} with FACS. Purified naive P14 CD8⁺ T cells
358 were resuspended in serum free DMEM and transferred by retro-orbital injection. For scRNA-seq
359 experiments during acute and chronic LCMV infection, 2x10⁴ naive P14 CD8⁺ T cells were transferred
360 per recipient mouse. For *Il2ra*^{-/-} single cell experiment, 2.4x10⁵ naive P14 CD8⁺ T cells were transferred
361 per recipient mouse (Thy1.1⁺ *Il2ra*^{-/-} to Thy1.1⁺ Thy1.2⁺ ratio = 2:1). For retroviral transduction, purified
362 naive CD8⁺ T cells were activated with anti-CD3 and anti-CD28, retrovirus was packaged and cells were
363 transduced as described²⁵ with the following modifications. Naive CD8 T cells were activated for 16-18
364 hours, transduced for 4 hours with retroviral supernatants, and immediately transferred to naive 6-8 week
365 old C57BL/6J hosts. 50,000 cells were transferred to each host and were infected with 2x10⁵ PFU of
366 LCMV_{Arm}, or 500,000 cells were transferred and hosts were administered IP injection of 1.5x10⁵ PFU of
367 LCMV_{Cl13}, or 1x10⁴ CFU of LM_{GP33}. LCMV_{Arm}, LCMV_{Cl13} and LM_{GP33} stocks were produced as
368 described²⁵. Infections were administered ~1 hour after adoptive transfer of transduced T cells, or the
369 following day(s) after naive cell transfer. Virus stocks were stored at -80°C and thawed immediately
370 before dilution. IP injection of 2x10⁵ PFU of LCMV_{Arm} per mouse was used to initiate acute infection,
371 and retroorbital injection of 2x10⁶ PFU LCMV_{Cl13} per mouse was used to initiate chronic infection.

372

373 **Flow cytometry analysis and Sorting for single cell sequencing**

374 Single cell suspensions were prepared by disrupting spleen sections by pressing through 70 μ m
375 cell strainer in DMEM with 10% FBS. The splenocyte suspensions or heparinized peripheral blood
376 collections were pelleted and red blood cells were lysed using ACK buffer. Cells were resuspended in
377 FACS buffer, stained for surface proteins and then fixed in 2-4% PFA and permeabilized for intracellular
378 staining. Anti-mouse CD4 (RM4-5), CD8 (53-6.7), CD44 (IM7), CD62L (MEL-14), CD25 (3C7), CD127
379 (A7R34), KLRG1 (2F1/KLRG1), CD27 (LG.3A10), TCF-1 (S33-966), CX3CR1 (SA011F11) and were
380 purchased from Biolegend or BD Biosciences. Intracellular staining for TCF-1 was performed using the
381 Foxp3 transcription factor staining kit (eBioscience). For analysis of cells on days 3 or 4 of infection,
382 spleens were cut into 1-2mm pieces and digested with collagenase IV (100 U/mL, Worthington) and
383 DNase I (10 μ g/mL, Sigma) in complete T cell media for 10 min at 37°C on a nutator, then disrupted over
384 a 70 μ m cell strainer. For FACS isolation, CD8 $^{+}$ T cells were initially enriched from total splenocyte
385 preparations by negative selection with anti-CD4, anti-CD19, anti-B220 and anti-TER119 and magnetic
386 streptavidin beads (Stemcell Technologies). Enriched cells were pre-stained with GP33-AF488 tetramer
387 (NIH tetramer facility) to label endogenous LCMV-specific CD8 $^{+}$ T cells, followed by staining with CD8
388 (BV421), Thy1.1 (PE) and Thy1.2 (APC) to label donor P14 CD8 $^{+}$ T cells and the cells were sorted using
389 a BD FACS AriaTM Fusion.

390

391 ***In vivo* Pooled RNAi Screen**

392 The RNAi screen was performed and analyzed as shown in fig S4A-B and as previously
393 described¹⁴ with the following modifications and details. Naive P14 CD8 T cells were activated for 18
394 hours using plate bound anti-CD3 and soluble anti-CD28 and transduced for 4 hours in 96 well plates
395 before cells from all wells were pooled. Immediately after pooling (~24hrs post activation) aliquots of
396 500,000 cells were transferred into multiple naive host mice that were rested for ~1 hour after receiving
397 cells before inoculation with 1.5 \times 10⁵ PFU LCMV_{Cl13} per mouse, which induces an acute infection in this
398 setting¹⁴. Two entire biological replicates of the screen were performed and used for computational
399 analysis, and each replicate was screened in three pools. Each pool of shRNAmirs targeting CRFs was
400 generated from ~500 shRNAmirs shRNAmirs which also included a common set of control shRNAmirs.
401 Each pool was analyzed in 10 recipient mice to maintain 50-100-fold theoretical representation of each
402 shRNAmir after engraftment. For input samples, ~8 \times 10⁵ transduced cells were FACS-purified 48 hours
403 after transduction. Eight days following infection, 3-8 \times 10⁵ cells from each KLRG1/CD127 gate were
404 recovered by FACS from the spleens of infected mice. Genomic DNA was purified from each sample and
405 used as PCR template to generate libraries for high-throughput sequencing as described¹⁴. Sequencing
406 reads are mapped to library fasta file containing shRNA sequence information with custom blast pipeline.

407 Raw read counts for each shRNA are normalized to total counts, and quantiles of each shRNA were
408 calculated with negative binomial distribution. To calculate the effect size of shRNA in different cell
409 population, the difference between quantiles in different cell population (quantile shift) was calculated for
410 individual shNRAs. To sum up the effect of each gene, the quantile shift for all shRNAs towards each
411 gene were converted to Z-scores, which were averaged and adjusted by p-value (to account for the
412 consistency of effect) to generate the adjusted Z-Scores for ranking (fig S4B).

413

414 **Nascent RNA-seq analysis**

415 For nascent RNA-seq of *in vitro* activated CD8 T cells, chromatin-associated RNA was prepared
416 and total RNA-seq libraries were prepared and sequenced as described²⁵. Pair end fastq reads were
417 trimmed with “trim_galore --paired --length 24 --stringency 3”. Trimmed fastq reads were aligned to
418 GRCm38 genome with bowtie2 with parameters “-p 16 -X 2000 --fr”⁵⁷. Forward and reverse strand reads
419 were separated with samtools⁵⁸. Reads per transcript were counted with subread featureCounts⁵⁹. Counts
420 from forward and reverse strands were merged with custom python script. Differential analysis was
421 performed with DEseq2⁶⁰.

422

423 **Single cell RNA-seq library generation, sequencing and analysis**

424 To prepare barcoded scRNA-seq libraries from multiple libraries, anti-mouse mouse MHC H-2
425 hashtag antibodies (Biolegend TotalSeqTM) were used to label separate FACS-purified subsets which
426 were washed, counted and pooled to final concentration of ~1,600 cells/ul. A total of ~50,000 cells were
427 loaded into one lane of the single cell A chip kit (P/N 1000009). Single-cell gel beads in emulsion (GEM)
428 were generated using the 10X Chromium single cell controller (10X Genomics, Pleasanton, CA). Single-
429 cell GEM’s and sequencing libraries were generated using the Single-cell 3’ library and gel bead kit V2
430 (P/N 120267) according to manufacturer recommendations. The final library size distributions and
431 amounts were assessed using bioanalyzer analysis and further quantified with the NEBNext library
432 quantification kit (P/N E7630). The cDNA and HTO libraries were pooled 10:1 and sequenced to a depth
433 of 50,000 reads per cell for the cDNA and 2,000 reads per cell for the HTO library. Libraries were
434 sequenced on the Illumina NovaSeq with the following 10X read format; Read 1 25bp, index i7 8bp, and
435 Read 2 98bp. Around 500 - 1500 million reads were generated per experiment, yielding 60-90%
436 sequencing saturation and around 1500-3000 median genes per cell after alignment. For hashtag library
437 sequences, 60-75% antibody reads were mapped to cells (usable), yielding around 3000-6000 usable
438 antibody reads per cell.

439 Cellranger 3.0 was used for fastq generation (cellranger mkfastq) and counting (cellranger count).
440 Standard quality filtering was performed with Scanpy to remove genes expressed in less than 3 cells,
441 doublets or low read cells (with gene / count per cell cutoff), and cells with high mitochondria count
442 percentage ⁶¹. Demultiplexing of Biolegend hashtags was performed with a custom python script to
443 exclude doublets and dropouts. After quality filtering, reads were normalized to 10,000 per cell and
444 logarithmized. Highly variable genes were identified with scanpy.pp.highly_variable_genes and selected.
445 Count matrices were then regressed and scaled with scanpy.pp.regress_out and scanpy.pp.scale. Force-
446 directed embedding was generated after PCA (scanpy.tl.pca) and UMAP based nearest neighbor analysis
447 (scanpy.pp.neighbors). Louvain cluster extraction (scanpy.tl.louvain) was performed on force-directed
448 embedding and the extracted clusters were analyzed with PAGA (scanpy.pl.paga) for cluster correlations
449 ^{18 13}. For velocity-based analysis, Velocyto was used to generate spliced / unspliced count matrix ¹². The
450 resulting matrix was processed in scVelo for velocity analysis ¹¹. For correlation of independent scRNA-
451 seq experiments, HarmonyPy was used for batch effect removal on normalized and scaled count matrices
452 of experiments ⁶². Dimensionality reduction was performed on batch effect removed matrices with PCA,
453 followed by UMAP projection.

454

455 **ChIP-seq analysis**

456 Raw fastq files of ChIP-seq experiments were downloaded from GEO with SRA-Tools fastq-
457 dump. Trimming of fastq files were performed with trim_galore. Trimmed reads were aligned to
458 GRCm38 genome with bowtie2 ⁵⁷. Aligned sam file were sorted and filtered for PCR duplicates with
459 samtools. Blacklisted regions were filtered with bedtools ^{63,64}. Peaks were called with MACS2 and
460 annotated with R package ChIPSeeker ^{65,66}. All analytical codes for ChIP-seq are published on Github:
461 https://github.com/TCellResearchTeam/T_Cell_ChIP. Visualization of ChIP data is accessible on UCSC
462 Track Hub: T_cell_ATAC_ChIP_Pipkin.

463

464 **GSEA**

465 GSEA was performed with R package clusterProfiler ²⁰. GSEA signatures were downloaded or
466 generated from published datasets available from GEO database. All signatures and description are
467 available on https://github.com/TCellResearchTeam/T_cell_signature_Reference.

468 References

469 1 Akondy, R. S. *et al.* Origin and differentiation of human memory CD8 T cells after vaccination. *Nature*
470 2 **552**, 362-367, doi:10.1038/nature24633 (2017).

471 2 Jameson, S. C. & Masopust, D. Understanding Subset Diversity in T Cell Memory. *Immunity* **48**, 214-226,
472 doi:10.1016/j.jimmuni.2018.02.010 (2018).

473 3 McLane, L. M., Abdel-Hakeem, M. S. & Wherry, E. J. CD8 T Cell Exhaustion During Chronic Viral
474 Infection and Cancer. *Annu Rev Immunol* **37**, 457-495, doi:10.1146/annurev-immunol-041015-055318
475 (2019).

476 4 Chung, H. K., McDonald, B. & Kaech, S. M. The architectural design of CD8+ T cell responses in acute
477 and chronic infection: Parallel structures with divergent fates. *J Exp Med* **218**, doi:10.1084/jem.20201730
478 (2021).

479 5 Restifo, N. P. & Gattinoni, L. Lineage relationship of effector and memory T cells. *Curr Opin Immunol* **25**,
480 556-563, doi:10.1016/j.coi.2013.09.003 (2013).

481 6 Wherry, E. J. *et al.* Lineage relationship and protective immunity of memory CD8 T cell subsets. *Nature*
482 *immunology* **4**, 225-234, doi:10.1038/ni889 (2003).

483 7 Kaech, S. M. & Wherry, E. J. Heterogeneity and cell-fate decisions in effector and memory CD8+ T cell
484 differentiation during viral infection. *Immunity* **27**, 393-405, doi:S1074-7613(07)00410-4 [pii]
485 10.1016/j.jimmuni.2007.08.007 (2007).

486 8 Buchholz, V. R., Schumacher, T. N. & Busch, D. H. T Cell Fate at the Single-Cell Level. *Annu Rev*
487 *Immunol* **34**, 65-92, doi:10.1146/annurev-immunol-032414-112014 (2016).

488 9 Reiner, S. L. & Adams, W. C. Lymphocyte fate specification as a deterministic but highly plastic process.
489 *Nat Rev Immunol* **14**, 699-704, doi:10.1038/nri3734 (2014).

490 10 Rosato, P. C., Wijeyesinghe, S., Stolley, J. M. & Masopust, D. Integrating resident memory into T cell
491 differentiation models. *Curr Opin Immunol* **63**, 35-42, doi:10.1016/j.coi.2020.01.001 (2020).

492 11 Bergen, V., Lange, M., Peidli, S., Wolf, F. A. & Theis, F. J. Generalizing RNA velocity to transient cell
493 states through dynamical modeling. *Nat Biotechnol* **38**, 1408-1414, doi:10.1038/s41587-020-0591-3
494 (2020).

495 12 La Manno, G. *et al.* RNA velocity of single cells. *Nature* **560**, 494-498, doi:10.1038/s41586-018-0414-6
496 (2018).

497 13 Wolf, F. A. *et al.* PAGA: graph abstraction reconciles clustering with trajectory inference through a
498 topology preserving map of single cells. *Genome Biol* **20**, 59, doi:10.1186/s13059-019-1663-x (2019).

499 14 Chen, R. *et al.* *In vivo* RNA interference screens identify regulators of antiviral CD4(+) and CD8(+) T cell
500 differentiation. *Immunity* **41**, 325-338, doi:10.1016/j.jimmuni.2014.08.002 (2014).

501 15 Wherry, E. J., Blattman, J. N., Murali-Krishna, K., van der Most, R. & Ahmed, R. Viral persistence alters
502 CD8 T-cell immunodominance and tissue distribution and results in distinct stages of functional
503 impairment. *J Virol* **77**, 4911-4927 (2003).

504 16 D'Souza, W. N. & Hedrick, S. M. Cutting edge: latecomer CD8 T cells are imprinted with a unique
505 differentiation program. *J Immunol* **177**, 777-781, doi:10.4049/jimmunol.177.2.777 (2006).

506 17 Blondel, V. D., Guillaume, J. L., Lambiotte, R. & Lefebvre, E. Fast unfolding of communities in large
507 networks. *J Stat Mech-Theory E*, doi:Artn P10008
508 10.1088/1742-5468/2008/10/P10008 (2008).

509 18 Becht, E. *et al.* Dimensionality reduction for visualizing single-cell data using UMAP. *Nat Biotechnol* **37**,
510 38-44 (2019).

511 19 Subramanian, A. *et al.* Gene set enrichment analysis: a knowledge-based approach for interpreting genome-
512 wide expression profiles. *Proc Natl Acad Sci U S A* **102**, 15545-15550, doi:10.1073/pnas.0506580102
513 (2005).

514 20 Yu, G., Wang, L. G., Han, Y. & He, Q. Y. clusterProfiler: an R package for comparing biological themes
515 among gene clusters. *OMICS* **16**, 284-287, doi:10.1089/omi.2011.0118 (2012).

516 21 Best, J. A. *et al.* Transcriptional insights into the CD8(+) T cell response to infection and memory T cell
517 formation. *Nature immunology* **14**, 404-412, doi:10.1038/ni.2536 (2013).

518 22 Stauber, D. J., Debler, E. W., Horton, P. A., Smith, K. A. & Wilson, I. A. Crystal structure of the IL-2
519 signaling complex: paradigm for a heterotrimeric cytokine receptor. *Proc Natl Acad Sci U S A* **103**, 2788-
520 2793, doi:10.1073/pnas.0511161103 (2006).

521 23 Wang, X., Rickert, M. & Garcia, K. C. Structure of the quaternary complex of interleukin-2 with its alpha,
522 beta, and gamma receptors. *Science* **310**, 1159-1163, doi:10.1126/science.1117893 (2005).

523 24 Diao, H. & Pipkin, M. Stability and flexibility in chromatin structure and transcription underlies memory
524 CD8 T-cell differentiation. *F1000Res* **8**, doi:10.12688/f1000research.18211.1 (2019).
525 25 Wang, D. *et al.* The Transcription Factor Runx3 Establishes Chromatin Accessibility of cis-Regulatory
526 Landscapes that Drive Memory Cytotoxic T Lymphocyte Formation. *Immunity* **48**, 659-674 e656,
527 doi:10.1016/j.jimmuni.2018.03.028 (2018).
528 26 Kaech, S. M. & Cui, W. Transcriptional control of effector and memory CD8+ T cell differentiation.
529 *Nature reviews. Immunology* **12**, 749-761, doi:10.1038/nri3307 (2012).
530 27 Milner, J. J. & Goldrath, A. W. Transcriptional programming of tissue-resident memory CD8(+) T cells.
531 *Curr Opin Immunol* **51**, 162-169, doi:10.1016/j.co.2018.03.017 (2018).
532 28 Shu, J. *et al.* Induction of Pluripotency in Mouse Somatic Cells with Lineage Specifiers. *Cell* **153**, 963-975,
533 doi:10.1016/j.cell.2013.05.001 (2013).
534 29 Laslo, P. *et al.* Multilineage transcriptional priming and determination of alternate hematopoietic cell fates.
535 *Cell* **126**, 755-766, doi:10.1016/j.cell.2006.06.052 (2006).
536 30 Joshi, N. S. *et al.* Inflammation directs memory precursor and short-lived effector CD8(+) T cell fates via
537 the graded expression of T-bet transcription factor. *Immunity* **27**, 281-295,
538 doi:10.1016/j.jimmuni.2007.07.010 (2007).
539 31 Dominguez, C. X. *et al.* The transcription factors ZEB2 and T-bet cooperate to program cytotoxic T cell
540 terminal differentiation in response to LCMV viral infection. *J Exp Med* **212**, 2041-2056,
541 doi:10.1084/jem.20150186 (2015).
542 32 Omilusik, K. D. *et al.* Transcriptional repressor ZEB2 promotes terminal differentiation of CD8+ effector
543 and memory T cell populations during infection. *J Exp Med* **212**, 2027-2039, doi:10.1084/jem.20150194
544 (2015).
545 33 Beltra, J. C. *et al.* Developmental Relationships of Four Exhausted CD8(+) T Cell Subsets Reveals
546 Underlying Transcriptional and Epigenetic Landscape Control Mechanisms. *Immunity* **52**, 825-841 e828,
547 doi:10.1016/j.jimmuni.2020.04.014 (2020).
548 34 Milner, J. J. *et al.* Runx3 programs CD8(+) T cell residency in non-lymphoid tissues and tumours. *Nature*
549 **552**, 253-257, doi:10.1038/nature24993 (2017).
550 35 Alfei, F. *et al.* TOX reinforces the phenotype and longevity of exhausted T cells in chronic viral infection.
551 *Nature* **571**, 265-269, doi:10.1038/s41586-019-1326-9 (2019).
552 36 Khan, O. *et al.* TOX transcriptionally and epigenetically programs CD8(+) T cell exhaustion. *Nature* **571**,
553 211-218, doi:10.1038/s41586-019-1325-x (2019).
554 37 Yao, C. *et al.* Single-cell RNA-seq reveals TOX as a key regulator of CD8(+) T cell persistence in chronic
555 infection. *Nat Immunol* **20**, 890-901, doi:10.1038/s41590-019-0403-4 (2019).
556 38 Pipkin, M. E. Runx proteins and transcriptional mechanisms that govern memory CD8 T cell development.
557 *Immunol Rev* **300**, 100-124, doi:10.1111/imr.12954 (2021).
558 39 Wu, J. I., Lessard, J. & Crabtree, G. R. Understanding the words of chromatin regulation. *Cell* **136**, 200-
559 206, doi:10.1016/j.cell.2009.01.009 (2009).
560 40 Bajpai, R. *et al.* CHD7 cooperates with PBAF to control multipotent neural crest formation. *Nature* **463**,
561 958-962, doi:10.1038/nature08733 (2010).
562 41 Gennery, A. R. *et al.* Mutations in CHD7 in patients with CHARGE syndrome cause T-B + natural killer
563 cell + severe combined immune deficiency and may cause Omenn-like syndrome. *Clin Exp Immunol* **153**,
564 75-80, doi:10.1111/j.1365-2249.2008.03681.x (2008).
565 42 Hurd, E. A., Poucher, H. K., Cheng, K., Raphael, Y. & Martin, D. M. The ATP-dependent chromatin
566 remodeling enzyme CHD7 regulates pro-neural gene expression and neurogenesis in the inner ear.
567 *Development* **137**, 3139-3150, doi:10.1242/dev.047894 (2010).
568 43 Witzl, K., Cale, C. M., Pierce, C. M., Wilson, L. C. & Hennekam, R. C. Immunological abnormalities in
569 CHARGE syndrome. *Eur J Med Genet* **50**, 338-345, doi:10.1016/j.ejmg.2007.05.002 (2007).
570 44 Chi, T. H. *et al.* Reciprocal regulation of CD4/CD8 expression by SWI/SNF-like BAF complexes. *Nature*
571 **418**, 195-199, doi:10.1038/nature00876 (2002).
572 45 Mackay, L. K. *et al.* Hobit and Blimp1 instruct a universal transcriptional program of tissue residency in
573 lymphocytes. *Science* **352**, 459-463, doi:10.1126/science.aad2035 (2016).
574 46 Xin, A. *et al.* A molecular threshold for effector CD8(+) T cell differentiation controlled by transcription
575 factors Blimp-1 and T-bet. *Nat Immunol* **17**, 422-432, doi:10.1038/ni.3410 (2016).
576 47 Wu, T. *et al.* The TCF1-Bcl6 axis counteracts type I interferon to repress exhaustion and maintain T cell
577 stemness. *Science immunology* **1** (2016).

578 48 Keppler, S. J., Rosenits, K., Koegl, T., Vucikaja, S. & Aichele, P. Signal 3 cytokines as modulators of
579 primary immune responses during infections: the interplay of type I IFN and IL-12 in CD8 T cell
580 responses. *PLoS One* **7**, e40865, doi:10.1371/journal.pone.0040865 (2012).

581 49 Kurd, N. S. *et al.* Early precursors and molecular determinants of tissue-resident memory CD8(+) T
582 lymphocytes revealed by single-cell RNA sequencing. *Sci Immunol* **5**, doi:10.1126/sciimmunol.aaz6894
583 (2020).

584 50 Milner, J. J. *et al.* Heterogenous Populations of Tissue-Resident CD8(+) T Cells Are Generated in
585 Response to Infection and Malignancy. *Immunity* **52**, 808-824 e807, doi:10.1016/j.jimmuni.2020.04.007
586 (2020).

587 51 Fonseca, R. *et al.* Developmental plasticity allows outside-in immune responses by resident memory T
588 cells. *Nat Immunol* **21**, 412-421, doi:10.1038/s41590-020-0607-7 (2020).

589 52 Youngblood, B. *et al.* Effector CD8 T cells dedifferentiate into long-lived memory cells. *Nature* **552**, 404-
590 409, doi:10.1038/nature25144 (2017).

591 53 Pauken, K. E. *et al.* Epigenetic stability of exhausted T cells limits durability of reinvigoration by PD-1
592 blockade. *Science* **354**, 1160-1165, doi:10.1126/science.aaf2807 (2016).

593 54 Sen, D. R. *et al.* The epigenetic landscape of T cell exhaustion. *Science* **354**, 1165-1169,
594 doi:10.1126/science.aae0491 (2016).

595 55 Li, P. *et al.* STAT5-mediated chromatin interactions in superenhancers activate IL-2 highly inducible
596 genes: Functional dissection of the Il2ra gene locus. *Proceedings of the National Academy of Sciences* **114**,
597 12111-12119 (2017).

598 56 Rodda, L. B. *et al.* Single-Cell RNA Sequencing of Lymph Node Stromal Cells Reveals Niche-Associated
599 Heterogeneity. *Immunity* **48**, 1014-+, doi:10.1016/j.jimmuni.2018.04.006 (2018).

600 57 Langmead, B. & Salzberg, S. L. Fast gapped-read alignment with Bowtie 2. *Nat Methods* **9**, 357-359
601 (2012).

602 58 Li, H. *et al.* The sequence alignment/map format and SAMtools. *Bioinformatics* **25**, 2078-2079 (2009).

603 59 Liao, Y., Smyth, G. K. & Shi, W. The Subread aligner: fast, accurate and scalable read mapping by seed-
604 and-vote. *Nucleic acids research* **41**, e108-e108 (2013).

605 60 Love, M. I., Huber, W. & Anders, S. Moderated estimation of fold change and dispersion for RNA-seq data
606 with DESeq2. *Genome Biol* **15**, 550, doi:10.1186/s13059-014-0550-8 (2014).

607 61 Wolf, F. A., Angerer, P. & Theis, F. J. SCANPY: large-scale single-cell gene expression data analysis.
608 *Genome Biol* **19**, 15, doi:10.1186/s13059-017-1382-0 (2018).

609 62 Korsunsky, I. *et al.* Fast, sensitive and accurate integration of single-cell data with Harmony. *Nat Methods*
610 **16**, 1289-1296 (2019).

611 63 Amemiya, H. M., Kundaje, A. & Boyle, A. P. The ENCODE blacklist: identification of problematic
612 regions of the genome. *Scientific reports* **9**, 1-5 (2019).

613 64 Quinlan, A. R. & Hall, I. M. BEDTools: a flexible suite of utilities for comparing genomic features.
614 *Bioinformatics* **26**, 841-842 (2010).

615 65 Zhang, Y. *et al.* Model-based analysis of ChIP-Seq (MACS). *Genome Biol* **9**, R137, doi:10.1186/gb-2008-
616 9-9-r137 (2008).

617 66 Yu, G., Wang, L. G. & He, Q. Y. ChIPseeker: an R/Bioconductor package for ChIP peak annotation,
618 comparison and visualization. *Bioinformatics* **31**, 2382-2383, doi:10.1093/bioinformatics/btv145 (2015).

619

620

621 **Acknowledgments:** This work was supported by Scripps Florida via the State of Florida (M.S.S.),
622 U19AI109976 (S.C., A.W.G., and M.E.P.), P01AI145815 (S.C., A.W.G., and M.E.P.), and the
623 Frenchman's Creek Women for Cancer Research (M.E.P.). We thank the The NIH Tetramer Facility
624 which is supported by contract 75N93020D00005. We would like to thank Drs. Mark Sundrud, Kendall
625 Nettles, and John Chang for critically reading the manuscript.

626

627 **Author contributions:** H.D., M.E.P. and S.C. conceived the study. H.D. and M.E.P. wrote the
628 manuscript with help from A.W.G, S.C., J.J.M., and G.M.. H.D. performed bioinformatics analysis and
629 conducted experiments. R.C. conducted RNAi screen. T.C.V. performed initial analysis of RNAi screen.
630 R.C., D.W., S.T., M.A.F., J.K., P.K., A.J.G, C.T. and J.J.M. performed experiments and analysis. D.M.M.
631 provided insights and reagents related to Chd7.

632

633 **Declaration of interests:** The authors declare no competing interests.

634

635 **Figure 1. Naive CD8 T cells differentiate along a linear path into common effector and memory**
636 **progenitor (EMP) cells.**

637 (A) PAGA initialized force-directed (FA) embedding based on individual cell gene expression profile,
638 each dot represent one cell. PAGA connectivity analysis was performed on indicated clusters P0-P10.

639 Clusters were extracted by Louvain method based on neighborhood graph. Neighborhood graph was
640 calculated with UMAP algorithm.

641 (B) Top: PAGA connectivity graph, each node represent one cluster, node sizes represent relative cell
642 number of cluster, edge widths represent relative PAGA connectivity score. Bottom: heatmap of PAGA
643 connectivity score between clusters.

644 (C) PAGA initialized FA embedding, coloring cells based on origin: day5 /day8, naive (grey) / LCMV_{Arm}
645 (purple) / LCMV_{Cl13} (orange).

646 (D) GSEA of selected signatures for Louvain clusters, separating LCMV_{Arm} / LCMV_{Cl13}. GSEA analysis
647 performed on mean of normalized gene expression per cluster. NES represented by color, -log10(padj)
648 represented by dot size. Labels of clusters inferred by GSEA result. (See also fig S1 J-M)

649 (E) Mean of scaled expression, showing top signature genes of Louvain clusters. Signature genes were
650 selected based on multiple differential analysis (Wilcoxon rank sum test, t-test, t-test over estimated
651 variances) of cells within each cluster v.s. all others, with adjusted p-adj cutoff 0.05 (intersection of all
652 tests) and absolute log2 fold change cutoff 1. Chromatin remodeling factors, transcription factors and
653 surface proteins were selected from the genes that meet the statistical cutoffs for creating the signature
654 gene lists. (See also Table S1). Top 10 signature genes ranked by t-test scores are represented in heatmap.

655 (F) Expression of cell surface markers by CTV determined by flow cytometry. 50,000 P14 CD8 T cells
656 were transferred per recipient mice which were given LCMV_{Arm}. Naive cells (grey) and cells from day3
657 (blue) / day4 (purple) post infection are represented in plots.

658 (G) Raw expression (logarithmized and normalized) of selected genes.

659

660 **Figure 2. Disparate RNA velocities develop in individual EMP cells and initiate a branched**
661 **manifold that establishes T_{MEM} and T_{EX} cell diversity.**

662 (A) Stream plot of velocity embedded on PAGA initialized single cell projection, separating LCMV_{Arm} /
663 LCMV_{Cl13} (including naive cells in both conditions).

664 (B) Transition probability heatmap between clusters estimated by scVelo, separating LCMV_{Arm} /
665 LCMV_{Cl13}. Color represent transition probability from row cluster to column cluster.

666 (C) Inferred LCMV_{Arm} / LCMV_{Cl13} developmental trajectory by PAGA connectivity analysis, scVelo
667 transition probability, pseudo-time (see Table S1) and real time.

668 (D) Spliced transcript abundance (Ms) of representative genes for each of the four inferred trajectory in
669 LCMV_{Arm} / LCMV_{Cl13}.
670 (E) Single cell velocity of selected driver genes, separating LCMV_{Arm} / LCMV_{Cl13}. Potential driver genes
671 were identified by combining top likelihood genes from analysis of all cells or multiple pairs of clusters
672 with transitioning potential. Transcription factors, chromatin remodelers and surface receptors were
673 selected within the identified likelihood genes (See Table S3).
674

675 **Figure 3: IL-2R-dependent transcription establishes EMP cells and transcriptional heterogeneity.**
676 (A) Heatmap of spliced transcript abundance of EMP^{P2} signature driver genes. EMP^{P2} common driver
677 genes were defined as intersection between driver genes with likelihood > 0.25 in: all cells, P2-P4, P2-P5
678 and P2-P7 (Table S3) P2 signature driver genes were defined as intersection between P2 signature genes
679 (described in **Fig 1E** and Table S1) and EMP^{P2} common driver genes.
680 (B) Single cell normalized *Il2ra* transcript abundance, spliced (Ms) / unspliced (Mu).
681 (C) PAGA initialized FA embedding based on single cell cell gene expression profile for Exp-*Il2ra*.
682 PAGA connectivity analysis was performed on indicated clusters. Clusters were extracted from UMAP
683 neighbor graph by Louvain method.
684 (D) Correlation of clusters between acute v.s. chronic single cell experiment and Exp-*Il2ra*. Correlation
685 represented by mean UMAP nearest neighbor graph scores between clusters from two experiments.
686 UMAP projection of single cells from two experiments generated by Harmony integrated normalized
687 count matrix from both experiment.
688 (E) Transition probability between clusters in activated WT and *Il2ra*^{-/-} cells. Left: all single cells from
689 WT / *Il2ra*^{-/-} samples in PAGA projection. Right: transition probability heatmap.
690 (F) Percentage distribution in Louvain clusters for each cell type. Total percentage in all Louvain clusters
691 add up to 100% for each cell type.
692 (G) Signature gene heatmap for clusters (calculated for all cells, including naive, WT and *Il2ra*^{-/-}).
693 Method as described in **Fig 1E**.
694 (H) Heatmap of log2 fold change of WT versus *Il2ra*^{-/-} for selected differential genes. Genes were
695 selected from cluster signature gene list (described in **Fig 2G**). The genes with minimum expression of
696 0.0015 in at least one cluster and with absolute log2fc >= 2 in at least one cluster (WT versus *Il2ra*^{-/-})
697 were used.
698 (I) Differential analysis of transcript abundance comparing Exp-*Il2ra*^{P1} and Exp-*Il2ra*^{P2}. X-axis represents
699 log2 fold change, and the y-axis represents -log10(pvalue). The horizontal line indicates pval = 0.05. The
700 vertical lines indicates absolute log2fc = 1. T_{RM} and T_{SCM} signature genes are highlighted in yellow and
701 green respectively.

702 (J) Number of differential nascent transcripts (between WT and *Il2ra*^{-/-}) at different time points post
703 activation. Differential nascent transcript is determined by DESeq2 (padj < 0.05) .
704 (K) Differential analysis volcano plot of WT versus *Il2ra*^{-/-} at 48 hours post activation. The x-axis
705 represents log2 fold change, and y-axis represents -log10(pvalue). The horizontal line indicates pval =
706 0.05. The vertical lines indicates absolute log2fc = 1. T_{RM} and T_{SCM} signature genes are highlighted in
707 yellow and green respectively.

708

709 **Figure 4: Differential utilization of CRFs establishes antiviral CD8 T cell heterogeneity.**

710 (A) Pooled RNAi screen and analysis simplified schematic (detailed schematic in fig S4A-B).
711 (B-D) Ranked lists of adjusted RNA - effects for input versus output, MP versus TE, and EE versus
712 others. Red / blue highlight genes that are top / bottom quarter in effect ranking.
713 (E-F) Experiment characterizing endogeneous CD8⁺ T cells response to LCMV_{Arm} infection (day 8 pi), in
714 mice of Chd7^{fl/fl}, Chd7^{+/fl}, Chd7^{+/+} genotypes. (E) Total activated CD8 T cell number in spleens. (F)
715 Representative flow cytometry plots showing CD127 and KLRG1 staining, and summarized percentages
716 of cells in each category.
717 (G) Smarca4 and Chd7 velocity and spliced transcript abundance (Ms) in single cell projection, separating
718 LCMV_{Arm} / LCMV_{Cl13}.
719 (H) GSEA of shChd7 versus shCd4 (control) and shBrg1 versus shCd19 (control). Signatures: IL-2
720 regulated signatures / key CD8 transcription factor (TF) regulated signatures / CD8 phenotype signatures /
721 Best et. al. longitudinal expression dynamic gene signatures.
722 (I) Differential expression of selected genes. Heatmap showing log2 fold change of gene expression
723 comparing shChd7 versus shCd4 (control) or shBrg1 versus shCd19 (control).
724 (J-K) Comparison of T-bet expression and phenotype between shChd7 versus shCd4 (control) during
725 LCMV_{Arm} or Listeria infection. Top: representative and summarized T-bet MFI. Bottom: representative
726 flow cytometry plot showing CD127 and KLRG1 staining.
727 (L) Multidimensional scaling plot showing similarity / dis-similarity of Chd7^{fl/fl} versus Chd7^{+/+} cells in
728 different stages: naive / 48h post activation / day8 sorted subsets.
729 (M) Differential expression of selected genes. Heatmap showing log2 fold change of gene expression
730 between Chd7^{fl/fl} versus Chd7^{+/+} in day8 sorted subsets (TE, MP, EE).

731

732

733 **Figure S1. Unsupervised approach to define early developmental clusters of antiviral CD8 T cells**
734 **during acute and chronic viral infections at single cell level.**

735 (A) Schematic of acute v.s. chronic single cell experiment. Donor naive P14 Thy1.1 CD8⁺ T cells from
736 were isolated and transferred into 4 groups of WT recipient mice at day -1. LCMV_{Arm} and LCMV_{Cl13}
737 infections were given at either day 0 or day 3 for each group. P14 Thy1.1 donor CD8⁺ T cells and GP33
738 Tetramer⁺ endogenous LCMV responding CD8⁺ cells (Tet) were isolated at the same day for each group.
739 Cells of each different origin were hash-tagged and mixed for scRNAseq in the same batch.

740 (B) Schematic of bioinformatic analysis pipeline of acute v.s. chronic single cell experiment. 10x outputs
741 were converted to fastq files and counted for transcript abundance with Cellranger 3.0. Basic quality filter
742 and normalization was performed with Scanpy. Biolegend hashtags were demultiplexed with custom
743 python script. Outliers were detected with DBSCAN (scikit-learn). Cells from each condition were
744 resampled to 750 – 1250 cells condition. Dimensionality reduction (PCA, UMAP, Force Atlas), clustering
745 (Louvain) and cluster connectivity analysis (PAGA) were performed with Scanpy functions. The count
746 matrix was also processed with Velocyto to separate spliced and unspliced transcripts for further velocity
747 associated analysis with scVelo.

748 (C) Stacked bar chart showing composition by different cell type for each Louvain cluster P0-P10. For
749 each cluster, total percentages of all cell types add up to 100%.

750 (D) Heatmap showing percentage distribution in Louvain clusters for each cell type. For each cell type,
751 total percentage in all Louvain clusters add up to 100%.

752 (E) Heatmap represents similarity between cell types based on distribution in Louvain clusters estimated
753 by bhattacharyya coefficient.

754 (F) Chi-square analysis of distribution of day 5 LCMV_{Arm} / LCMV_{Cl13} P14 CD8⁺ cell distribution in / out
755 cluster P2.

756 (G) Violin plots of raw expression (logarithmized and normalized) per cluster for selected phenotype
757 marker genes.

758 (H) See **Fig 1E** description: mean of scaled expression heatmap, top 10 genes ranked by t-test score
759 plotted. Left: all cells; middle and right: separating LCMV_{Arm} / LCMV_{Cl13}.

760 (I) Phenotype correlation between CX3CR1 - CD27 and CD25 - TCF-1 of transferred P14 CD8⁺ cell day
761 4 post LCMV infection (50k cells transferred).

762 (J) (K) (L) (M) GSEA of selected signatures for Louvain clusters, separating LCMV_{Arm} / LCMV_{Cl13}.
763 GSEA analysis performed on mean of normalized gene expression per cluster. Colors of dots represent
764 NES, and sizes of dots represent -log10(padj) of signature enrichment. Best et. al. signatures annotated
765 with longitudinal expression dynamics of genes in the clusters and grouped based on expression dynamics
766 (plot from original publication).

767

768 **Figure S2. Single cell RNA velocity and root / terminal score indicates P2 & P5 are developmental**
769 **roots.**

770 (A) Single cell velocity vectors for each cluster.

771 (B)(C) Root / terminal score analysis, separating LCMV_{Arm} / LCMV_{Cl13} (not including naive cells). Top:
772 Root / terminal score of single cells, overlayed with grid velocity. Bottom: average root / terminal per
773 cluster.

774 (D)(E) Single cell spliced transcript abundance / unspliced transcript abundance for selected driver genes,
775 Separating LCMV_{Arm} / LCMV_{Cl13}.

776 (F) GSEA analysis of P14 Runx3^{-/-} versus WT CD8 T cell gene expression, at day 5 / day 8 p.i. LCMV
777 infection. Positive NES scores indicate signature genes more highly expressed in Runx3^{-/-} comparing with
778 WT; negative NES scores indicate signature genes more highly expressed in WT comparing with Runx3^{-/-}.
779

780 **Figure S3. IL-2 signaling contribute to EMP formation via transcription regulation**

781 (A) Schematic of Exp-*Il2ra*: *Il2ra*^{-/-} and WT P14 CD8⁺ T cell cogenetic transfer and single cell
782 experiment.

783 (B) Left: PAGA connectivity graph, each node represent one cluster, node sizes represent relative cell
784 number of cluster, edge widths represent relative PAGA connectivity score. Middle: heatmap of PAGA
785 connectivity score between clusters. Right: Stacked bar chart showing composition by different cell type
786 for each Louvain clusters. For each cluster, total percentages of all cell types add up to 100%.

787 (C) Exp-*Il2ra* PAGA initialized FA embedding, highlighting cells of different origin.

788 (D) Terminal score of *Il2ra*^{-/-} single cells in Exp-*Il2ra*.

789 (E) Chi-square analysis of cell type distribution in Exp-*Il2ra*. Top: Cell number distribution in activated
790 clusters in Exp-*Il2ra*^{P1} or outside of Exp-*Il2ra*^{P1} for WT and *Il2ra*^{-/-}. Bottom: Cell number distribution in
791 activated clusters except for P1, comparing WT and *Il2ra*^{-/-}.

792 (F) GSEA of T_{RM} gene signature in Exp-*Il2ra*^{P5} WT versus *Il2ra*^{-/-}.

793 (G) Differential expression volcano plot of WT and *Il2ra*^{-/-} in Exp-*Il2ra*^{P2}. The x-axis represents log2 fold
794 change, and y-axis represents -log10(pvalue). The horizontal line indicates pval = 0.05. The vertical lines
795 indicates absolute log2fc = 1. TE signature genes marked in green.

796 (H) Schematic of *Il2ra*^{-/-} and WT P14 CD8⁺ T cell *in vitro* activation and nascent RNA-seq experiment.

797 (I) See **Fig 3H**. Dark red and dark blue area represent number of genes genes that are expressed higher in
798 WT than *Il2ra*^{-/-} which are upregulated post activation (each time point versus naive), or genes expressed
799 lower in WT than *Il2ra*^{-/-} which are downregulated post activation.

800 (J) GSEA of T_{SCM} signature indicates that $Il2ra^{-/-}$ express T_{SCM} signature genes at higher level than WT at
801 48h post activation.
802 (K) GSEA enrichment of IL-2 promoted / repressed genes in $Exp-Il2ra^{P3}$ (EMP) versus $Exp-Il2ra^{P1}$
803 (Arrested) differential gene list (signature genes selected from DEseq2 analysis of 48h post activation,
804 WT versus $Il2ra^{-/-}$ with cutoffs $padj < 0.05$, absolute log2 fold change > 1.2).
805 (L) Venn diagrams showing overlap between P2 $LCMV_{Arm}$ and $LCMV_{Cl13}$ differential genes ($padj < 0.05$)
806 and IL2-Stat5 promoted / repressed genes. Pie charts showing the percentage of Stat3 bound genes in the
807 intersection of $LCMV_{Arm}$ and $LCMV_{Cl13}$ differential genes and IL2-Stat5 promoted / repressed genes.
808 IL2-Stat5 promoted genes: nascent transcript abundance WT $> Il2ra^{-/-}$ and WT 48h $>$ WT 6h (DESeq2,
809 pvalue ≤ 0.05), intersected with genes that are bound by Stat5¹. IL2-Stat5 repressed genes: nascent
810 transcript abundance WT $< Il2ra^{-/-}$ and WT 48h $<$ WT 6h (DESeq2, pvalue ≤ 0.05), intersected with
811 genes that are bound by Stat5.
812 (M) GSEA enrichment of IL2 repressed signature between $LCMV_{Arm}$ and $LCMV_{Cl13}$ differential velocity
813 genes in EMP^{P2}.
814 (N) GSEA enrichment of 48h IL2 repressed signature (described in fig S3K) in pT_{SCM}^{P7} versus EMP^{P2},
815 separating $LCMV_{Arm}$ and $LCMV_{Cl13}$.
816 (O) Visualization of ChIP-seq, ATAC-seq and nascent RNA-seq tracks at *Il6st* and *Bcl6* regions.
817 Asterisks represent significant peaks (MACS2, q-value < 0.01).
818

819 **Figure S4. Identification and functional analysis of CRFs that is required for CD8⁺ T cell lineage
820 formation**

821 (A) Experimental setup of CRF RNAi screen (See **Methods**).
822 (B) Bioinformatic analysis pipeline of CRF RNAi screen (See **Methods**).
823 (C) Flow cytometry at day5 pi showing $KLRG1^{hi}$ population in $Chd7^{fl/fl}$ is reduced comparing with
824 $Chd7^{+/+}$.
825 (D)(E) Flow cytometry of transduced and transferred P14 CD8 T cells post $LCMV_{Arm}$ infection. CD8 T
826 cells were simultaneously transduced with a combination of retroviral vectors containing shCd4
827 (Ametrine, control) and empty vector (GFP, control), or a combination of retroviral vectors containing
828 shSmarca4 / shChd7 (Ametrine) and T-bet cDNA (GFP). Phenotypes of RNAi and T-bet overexpression
829 were accessed by flow cytometry at day8 pi.
830 (F)(G)(H) Ranked lists of adjusted RNA - effects for input versus output, MP versus TE, and EE versus
831 others (as described in fig 5B-D), annotating genes from major CRF families.
832 (I) Six major clusters of CRFs extracted from hierarchical clustering of CRFs based on RNAi effect
833 scores of 3 categories (MP v.s. TE, EE v.s. Other, Input v.s. Output) from screen.

834 (J)(K) Flow cytometry of splenic CD8⁺ T cell phenotype day8 pi LCMV_{Arm}, comparing transferred P14
835 CD8⁺ T cells transduced with shCd4(control) and multiple shRNAs against Carm1 and Prmt5.
836 (L) Flow cytometry of peripheral blood CD8⁺ T cell phenotype day7 and day12 pi LCMV_{Arm}, comparing
837 congenially transferred P14 CD8⁺ T cells transduced with shCd19(control) and shTaf1.

838

839 **Table S1.**

840 Acute versus Chronic infection (LCMV_{Arm} / LCMV_{C113}) single cell experiment - clusters and cluster
841 signature genes

842

843 **Table S2.**

844 GSEA signatures

845

846 **Table S3.**

847 Acute versus Chronic infection (LCMV_{Arm} / LCMV_{C113}) single cell experiment - differential expression
848 of genes between LCMV_{Arm} and LCMV_{C113}

849

850 **Table S4.**

851 Acute versus Chronic infection (LCMV_{Arm} / LCMV_{C113}) single cell experiment - scVelo likelihood genes
852

853 **Table S5.**

854 Acute versus Chronic infection (LCMV_{Arm} / LCMV_{C113}) single cell experiment - spliced / unspliced
855 transcript abundance and velocity of likelihood genes

856

857 **Table S6.**

858 Exp-*Il2ra* - clusters and cluster signature genes

859

860 **Table S7.**

861 RNAi screen of chromatin remodelers: shRNA sequences; scores of each gene in different comparisons

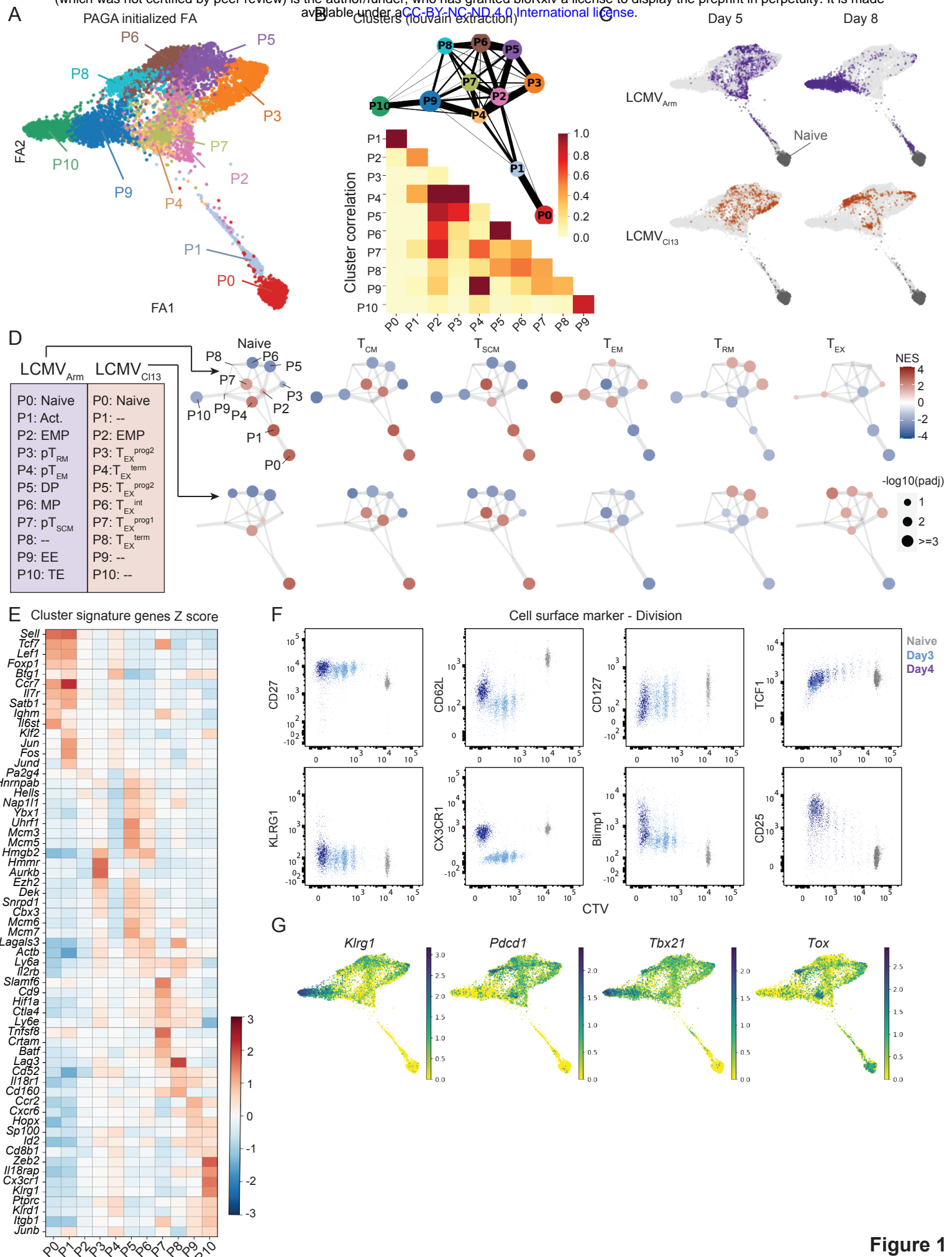
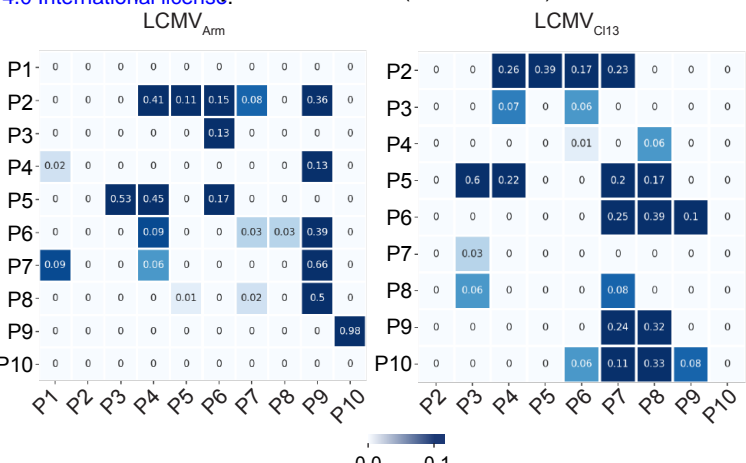
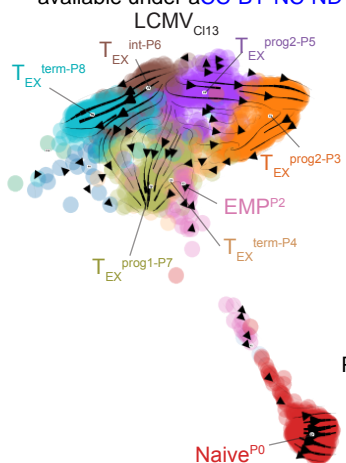
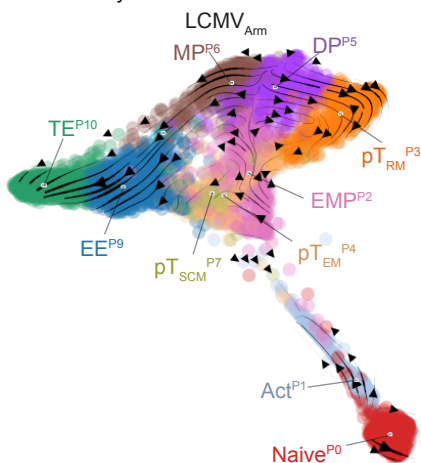
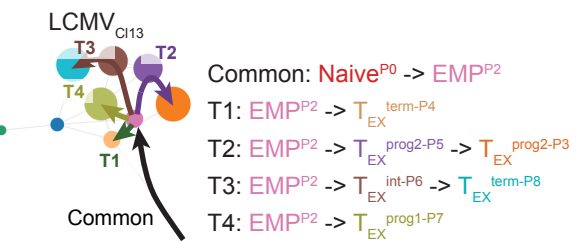
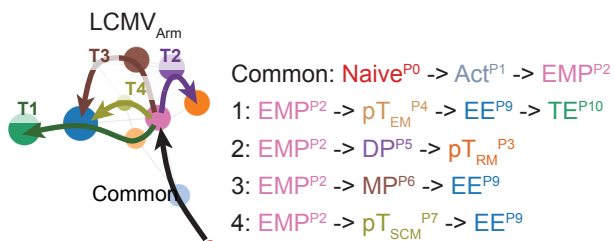


Figure 1

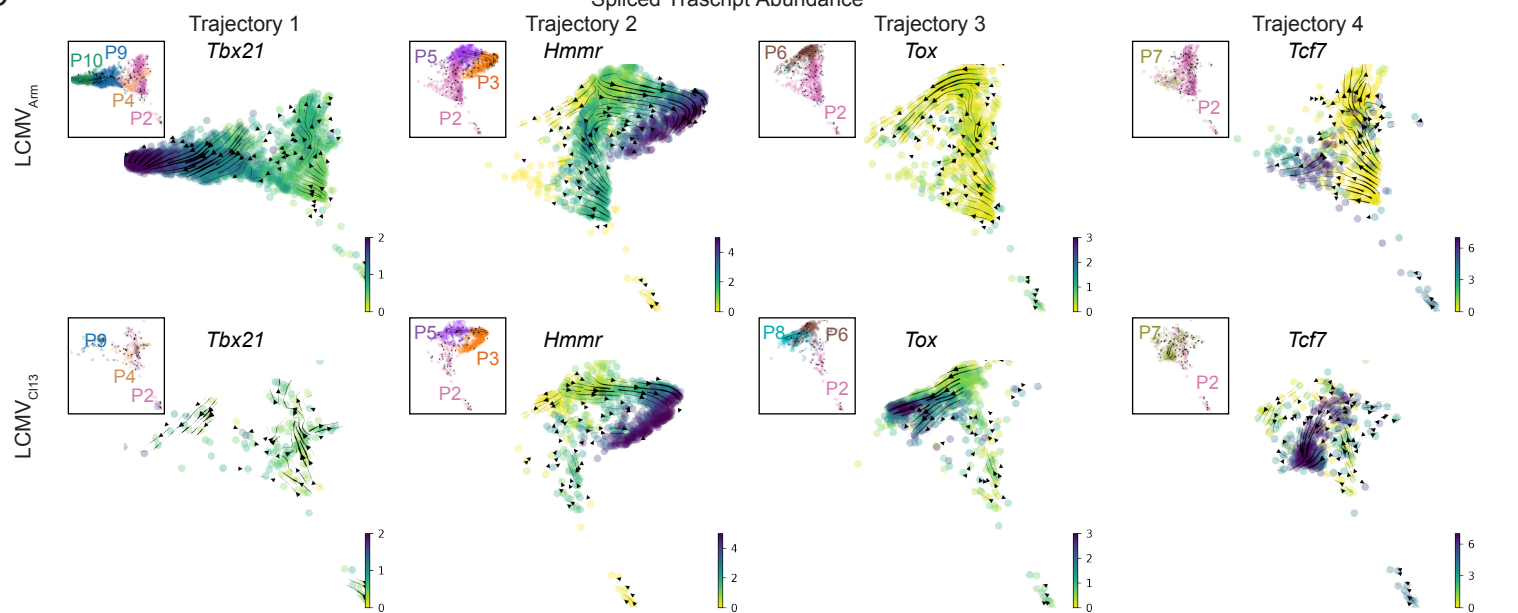
A Velocity transition stream



C



D



E

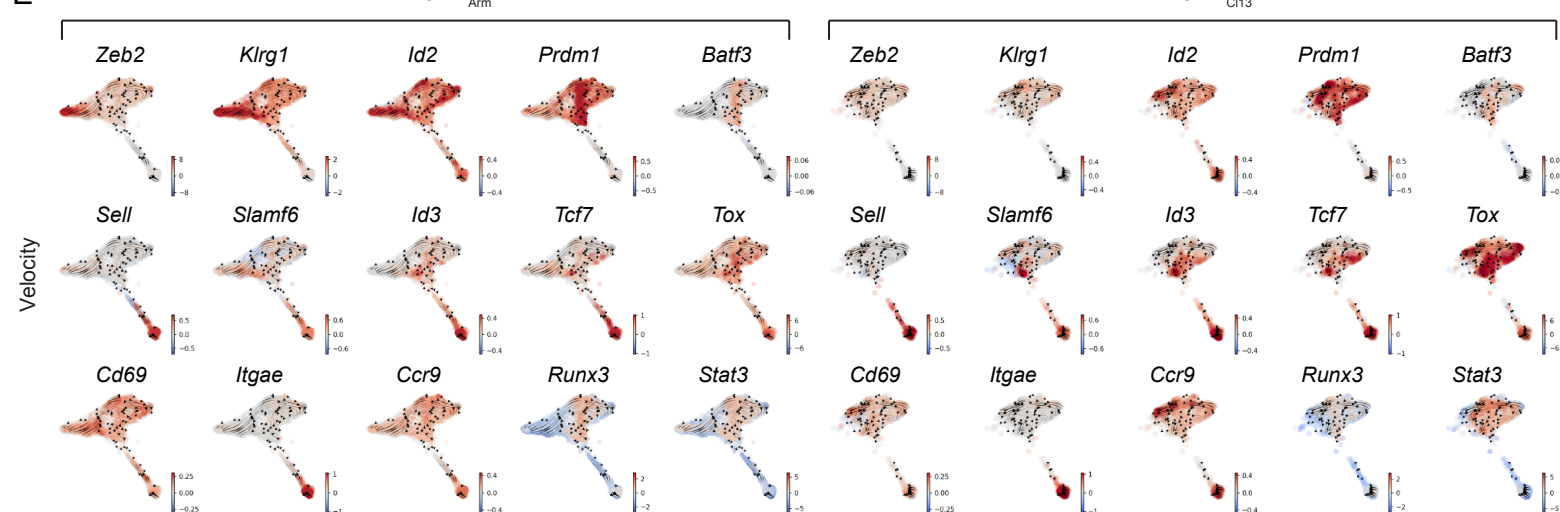


Figure 2

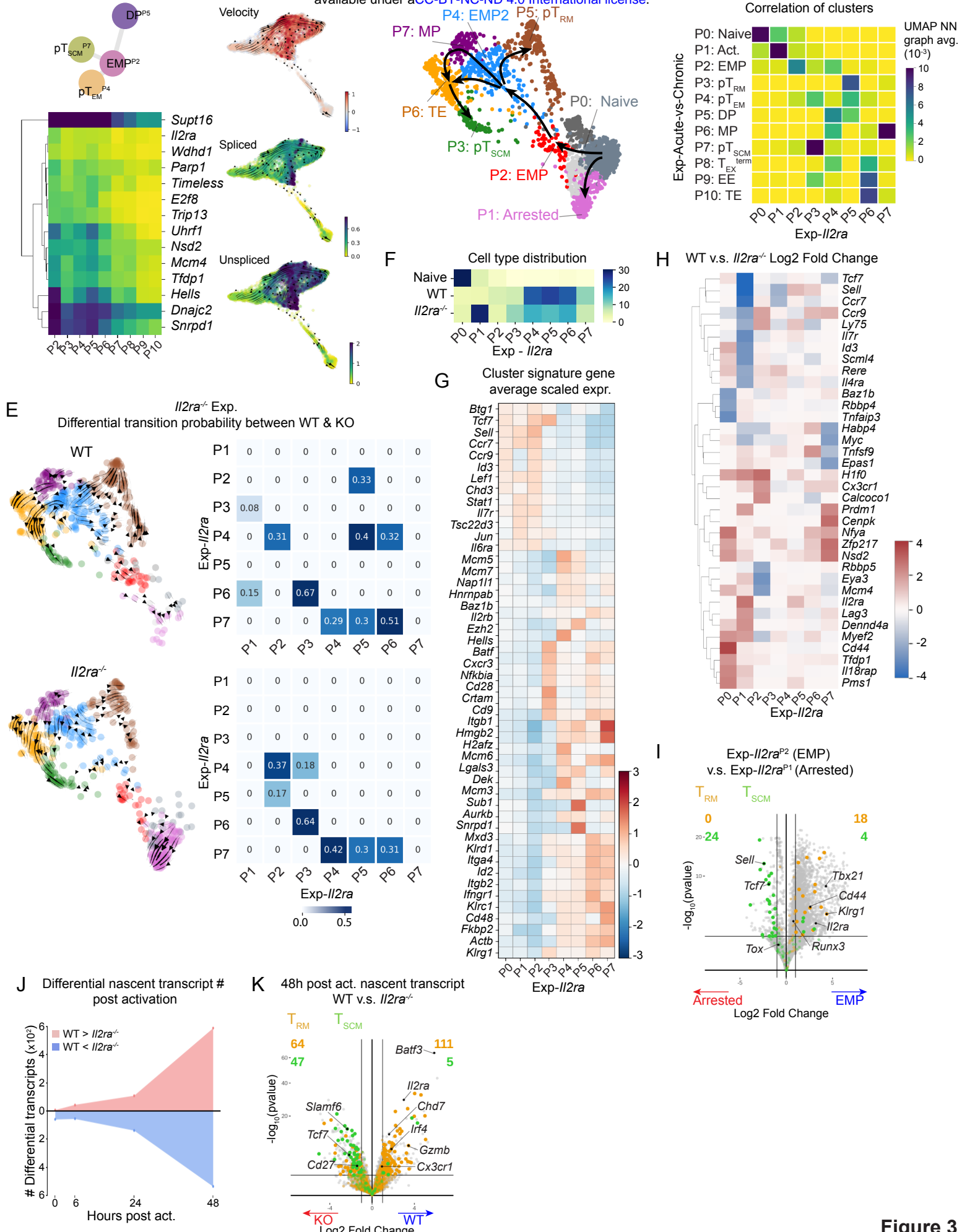
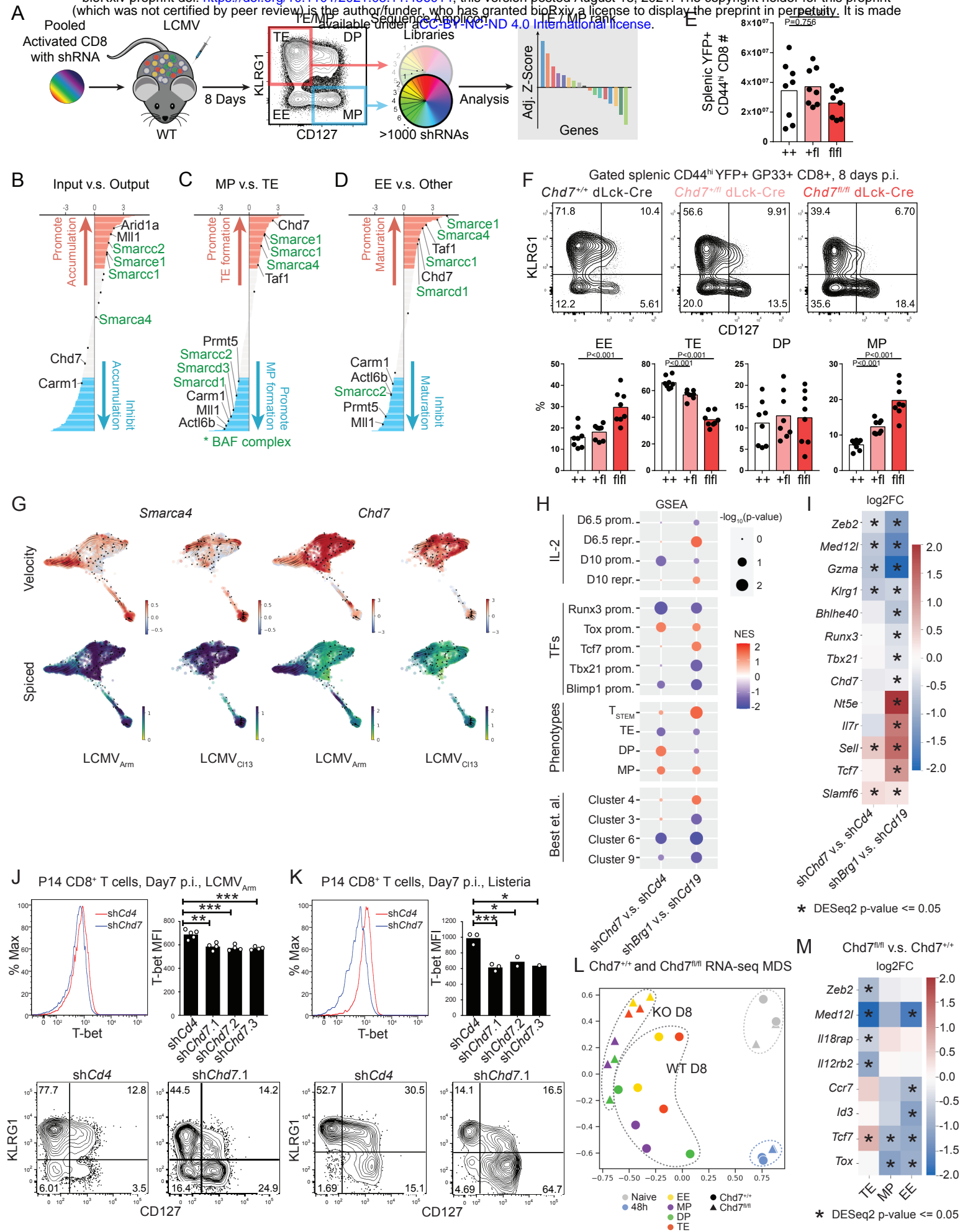
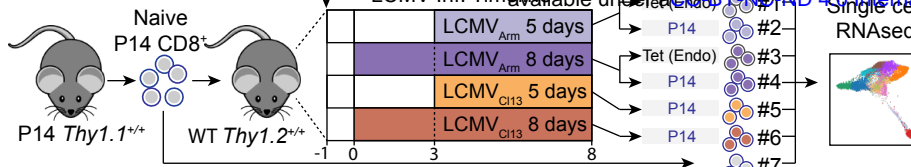


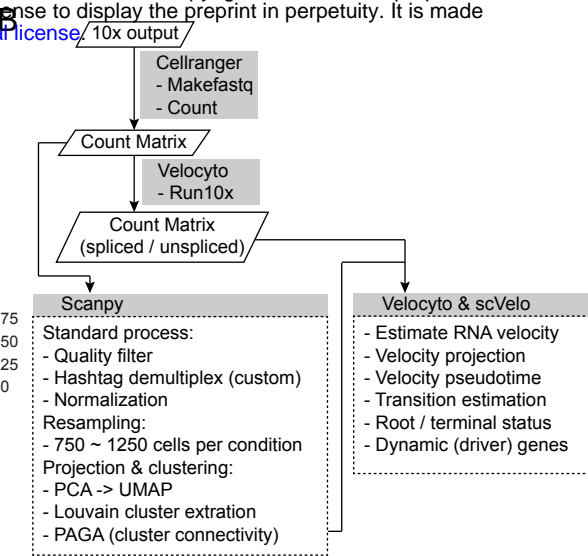
Figure 3



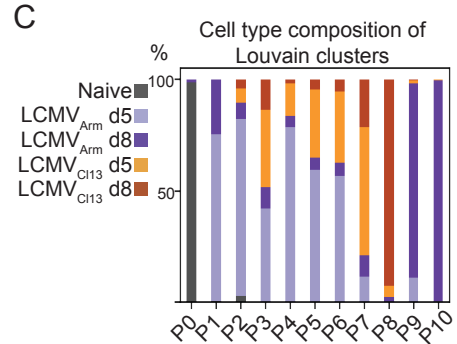
A



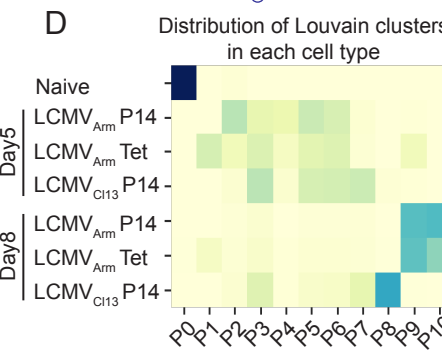
B



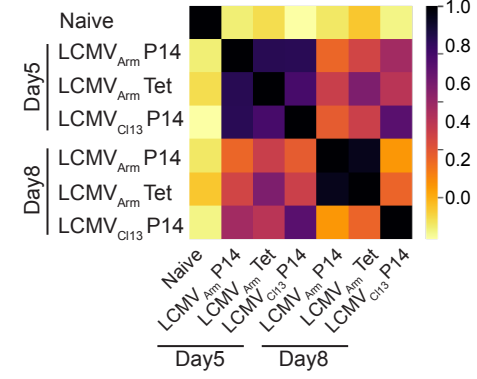
C



D



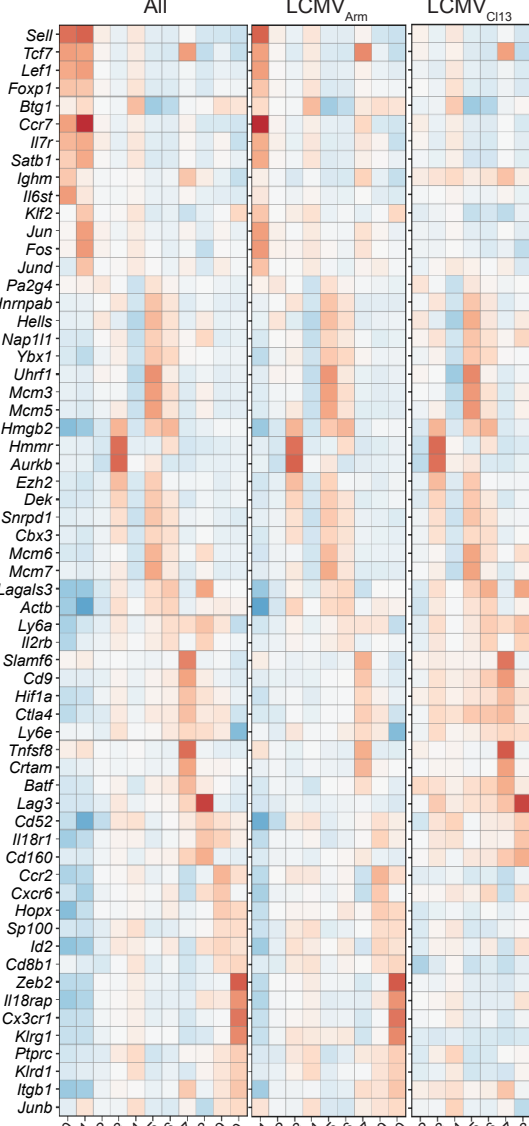
E Cell type similarity in cluster distribution (Bhattacharyya coefficient)



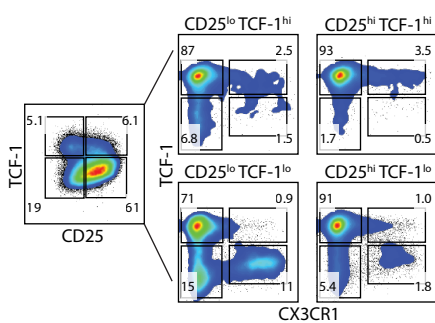
F

	P2	Other	
LCMV _{Arm}	338 (27%)	912 (73%)	1250
LCMV _{Cl13}	36 (3%)	1214 (97%)	1250
	374	2126	
Chisq:	286.76		
p-value:	< 0.00001		

H Louvain cluster signature genes (Scaled Expression)

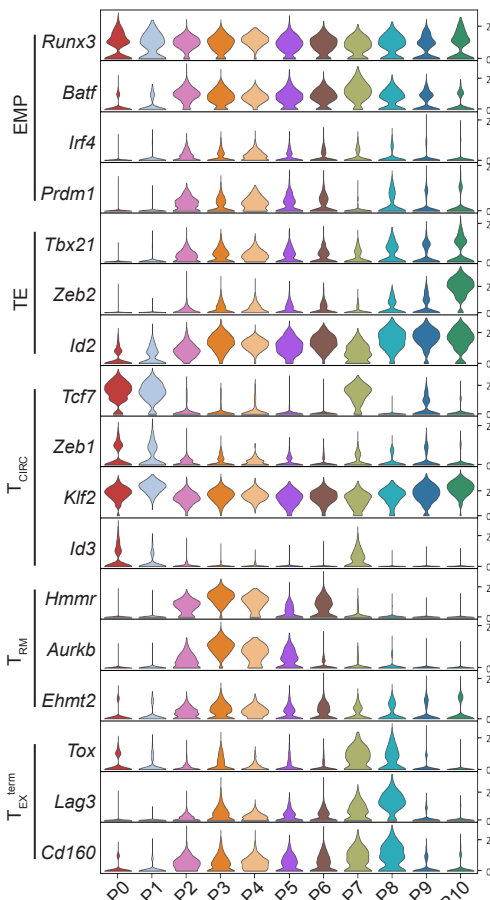


I



G

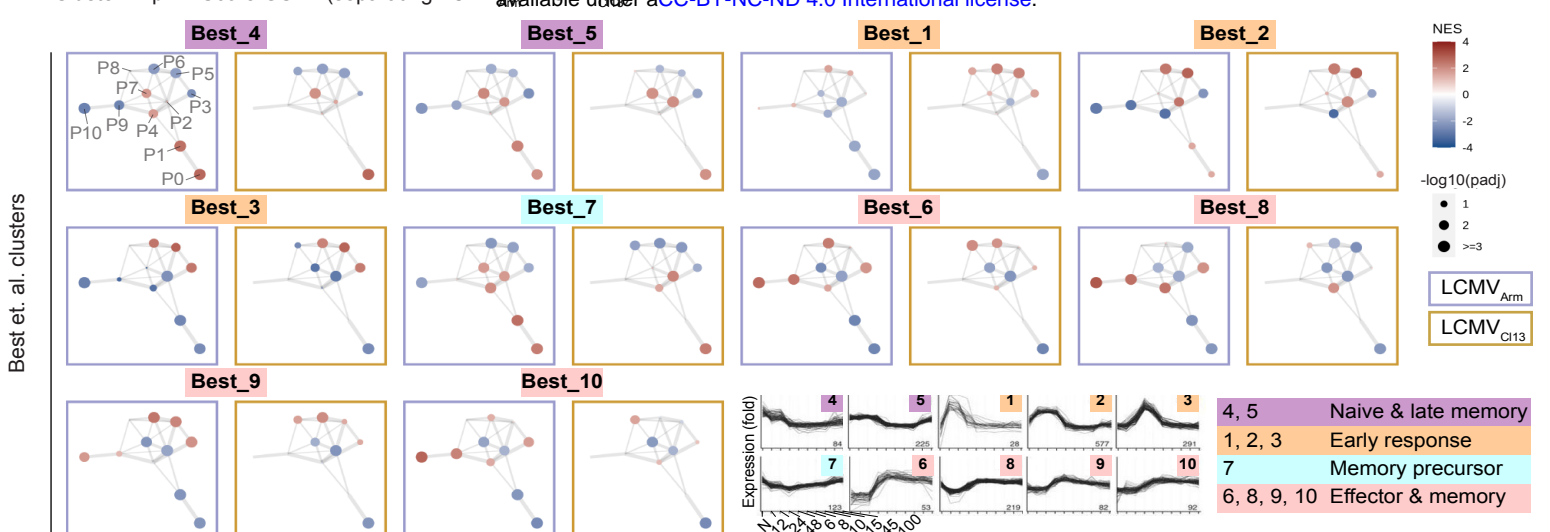
Normalized Expr.



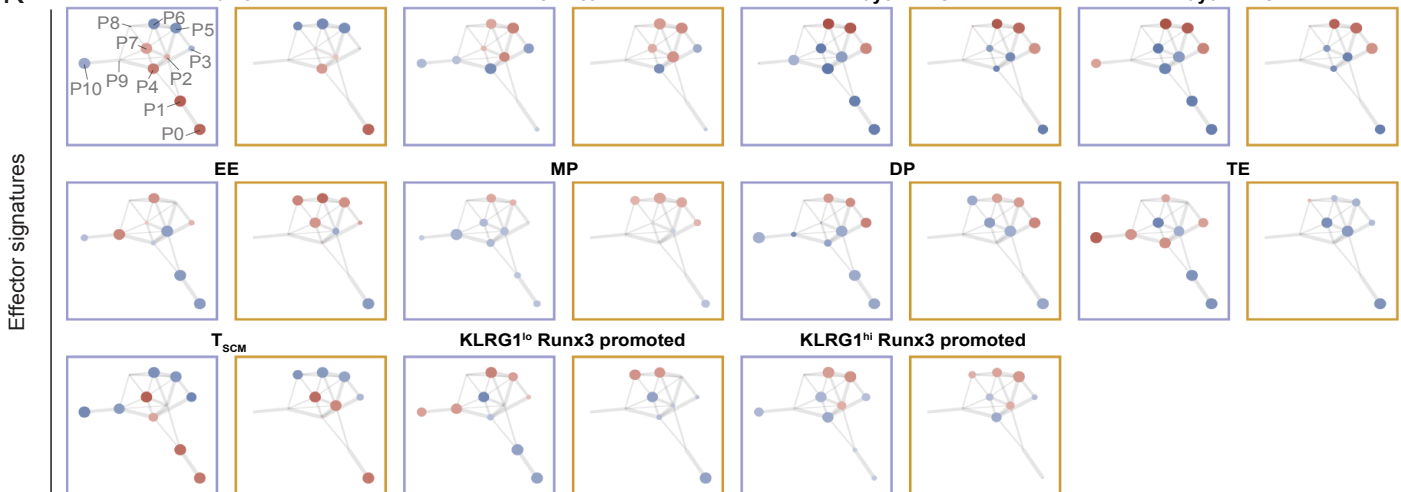
LCMV _{Arm}	LCMV _{Cl13}
P0: Naive	P0: Naive
P1: Act.	P1: --
P2: EMP	P2: EMP
P3: pT _{RM}	P3: T _{EX} prog2
P4: pT _{EM}	P4: T _{EX} term
P5: DP	P5: T _{EX} prog2
P6: MP	P6: T _{EX} int
P7: pT _{SCM}	P7: T _{EX} prog1
P8: --	P8: T _{EX} term
P9: EE	P9: --
P10: TE	P10: --

Figure S1

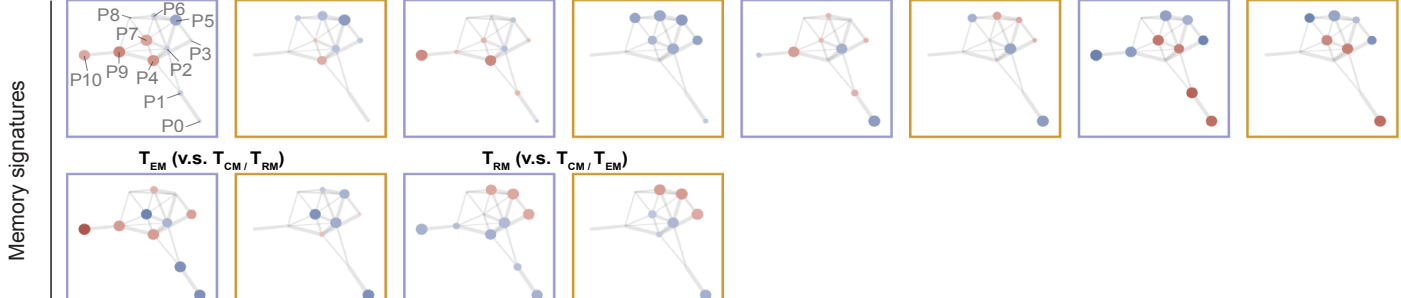
J



K



L



M

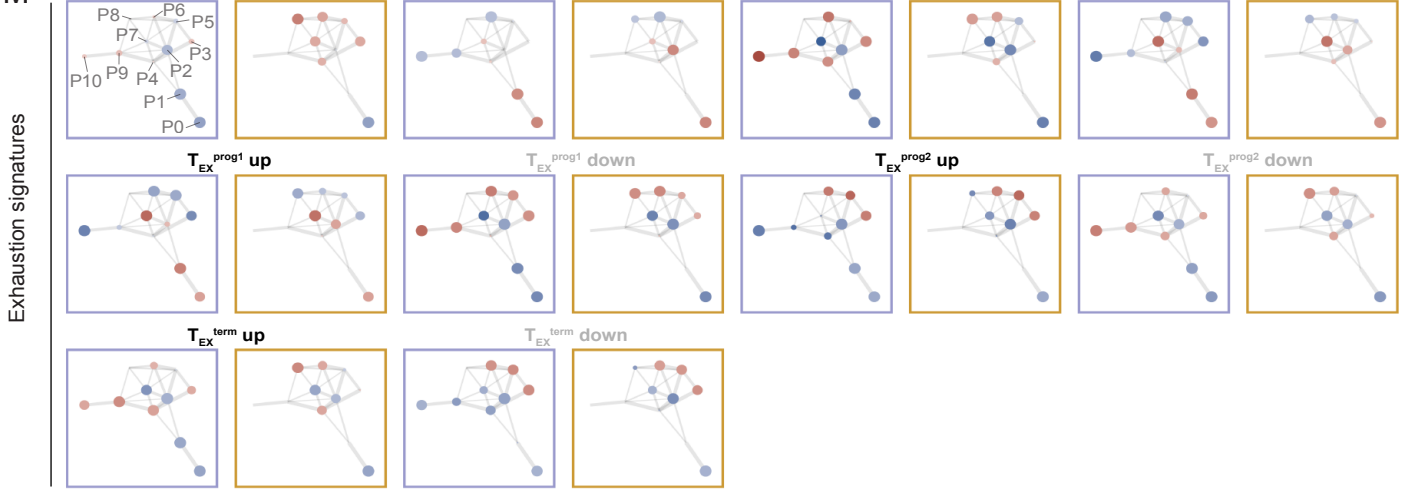


Figure S1

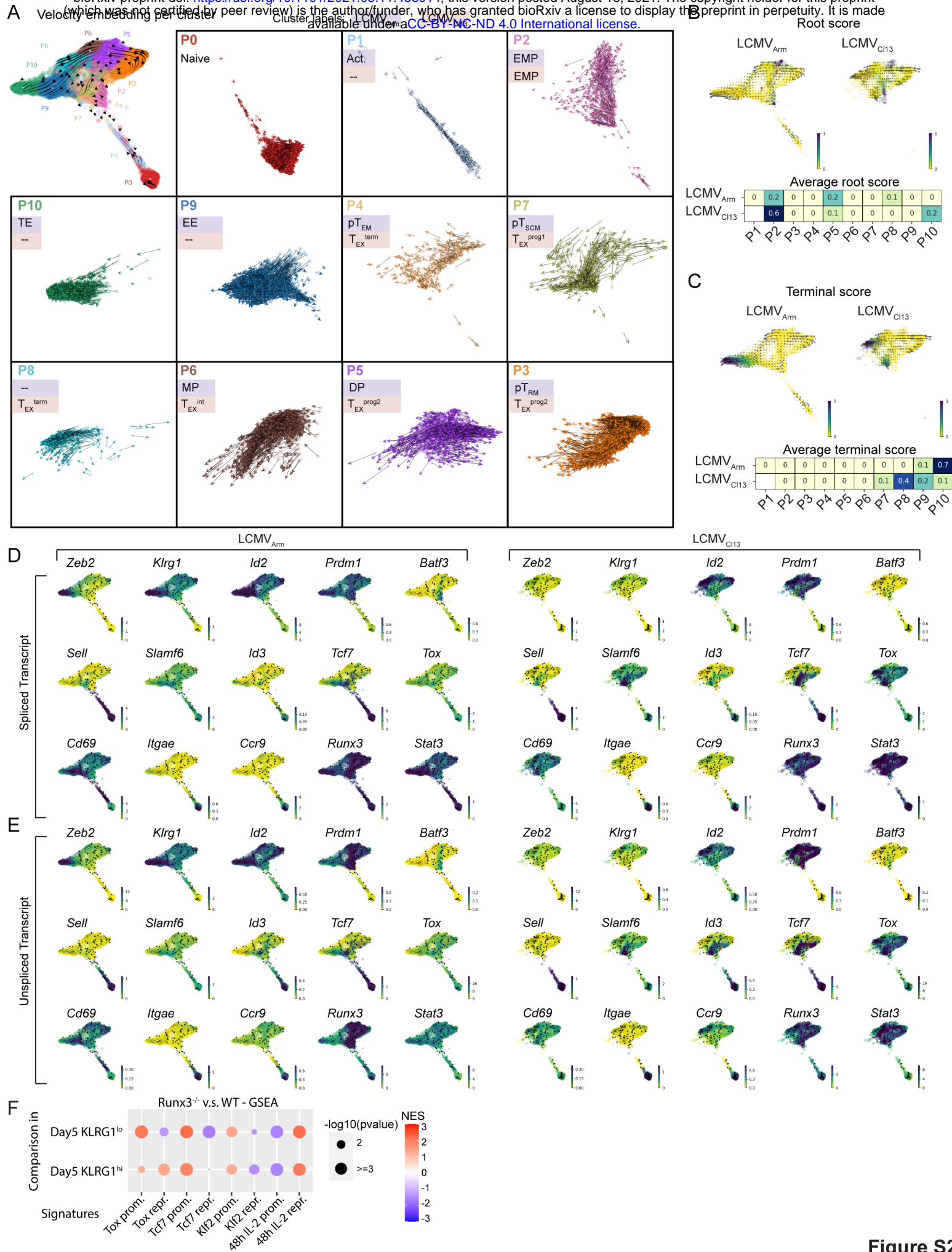
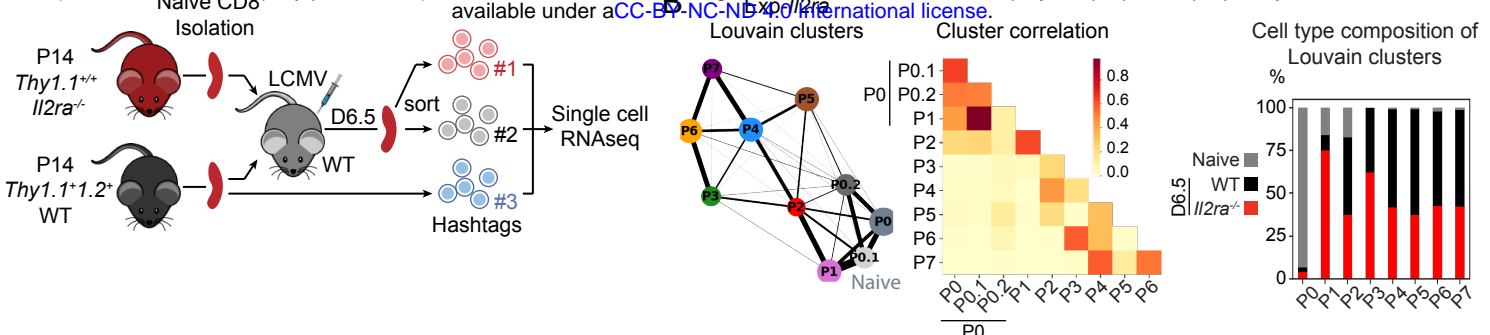
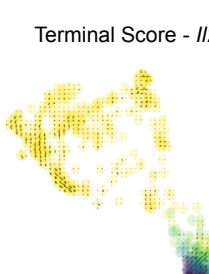
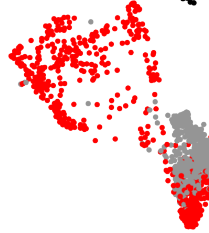
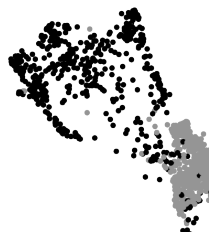


Figure S2

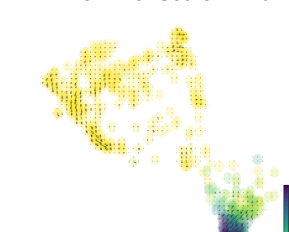
A



C ● Naive ● WT ● $\text{II}2\text{ra}^{-/-}$

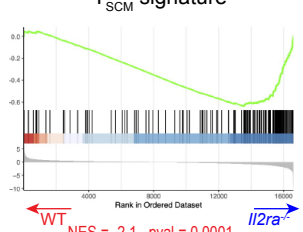


D Terminal Score - $\text{II}2\text{ra}^{-/-}$



J GSEA in 48h Act. $\text{II}2\text{ra}^{-/-}$ v.s. WT

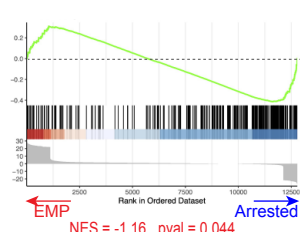
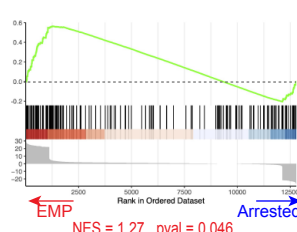
T_{SCM} signature



K

IL2 regulated signature enrichment in
Exp- $\text{II}2\text{ra}^{P2}$ (EMP) v.s. Exp- $\text{II}2\text{ra}^{P1}$ (Arrested)

IL2 promoted IL2 repressed



E

Exp- $\text{II}2\text{ra}^{-/-}$

Chi-square Distribution analysis

Cell # in activated clusters (exclude P0: Naive)

	P1: Arrested	Other	
WT	18 (3.7%)	464 (96.3%)	482
$\text{II}2\text{ra}^{-/-}$	155 (30.0%)	361 (70.0%)	516
	173	825	
Chisq:	118.5		
p-value:	1.35×10^{-27}		

Cell # in activated clusters (exclude P0 & P1)

	P3	Other	
WT	33 (7.1%)	431 (92.9%)	464
$\text{II}2\text{ra}^{-/-}$	54 (15.0%)	307 (85.0%)	361
	87	738	
Chisq:	12.4		
p-value:	0.00042		

	P5	Other	
WT	124 (26.7%)	340 (73.3%)	464
$\text{II}2\text{ra}^{-/-}$	75 (20.8%)	286 (79.2%)	361
	199	626	
Chisq:	3.6		
p-value:	0.057		

F

Exp- $\text{II}2\text{ra}^{P5}$ (pT_{RM})

WT v.s. $\text{II}2\text{ra}^{-/-}$

TRM biased signature

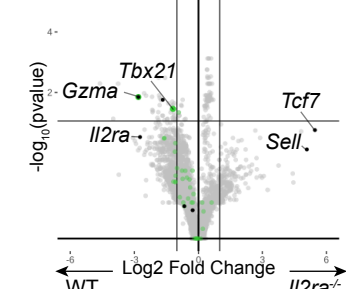


G

Exp- $\text{II}2\text{ra}^{P2}$ (EMP)

$\text{II}2\text{ra}^{-/-}$ v.s. WT

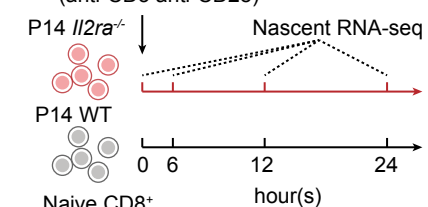
TE signature



H

In vitro TCR stimu.

(anti-CD3 anti-CD28)



I Differential nascent transcript # post activation WT v.s. $\text{II}2\text{ra}^{-/-}$

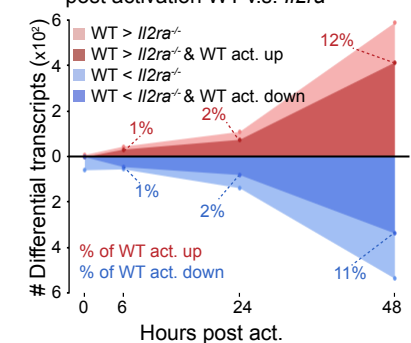


Figure S3

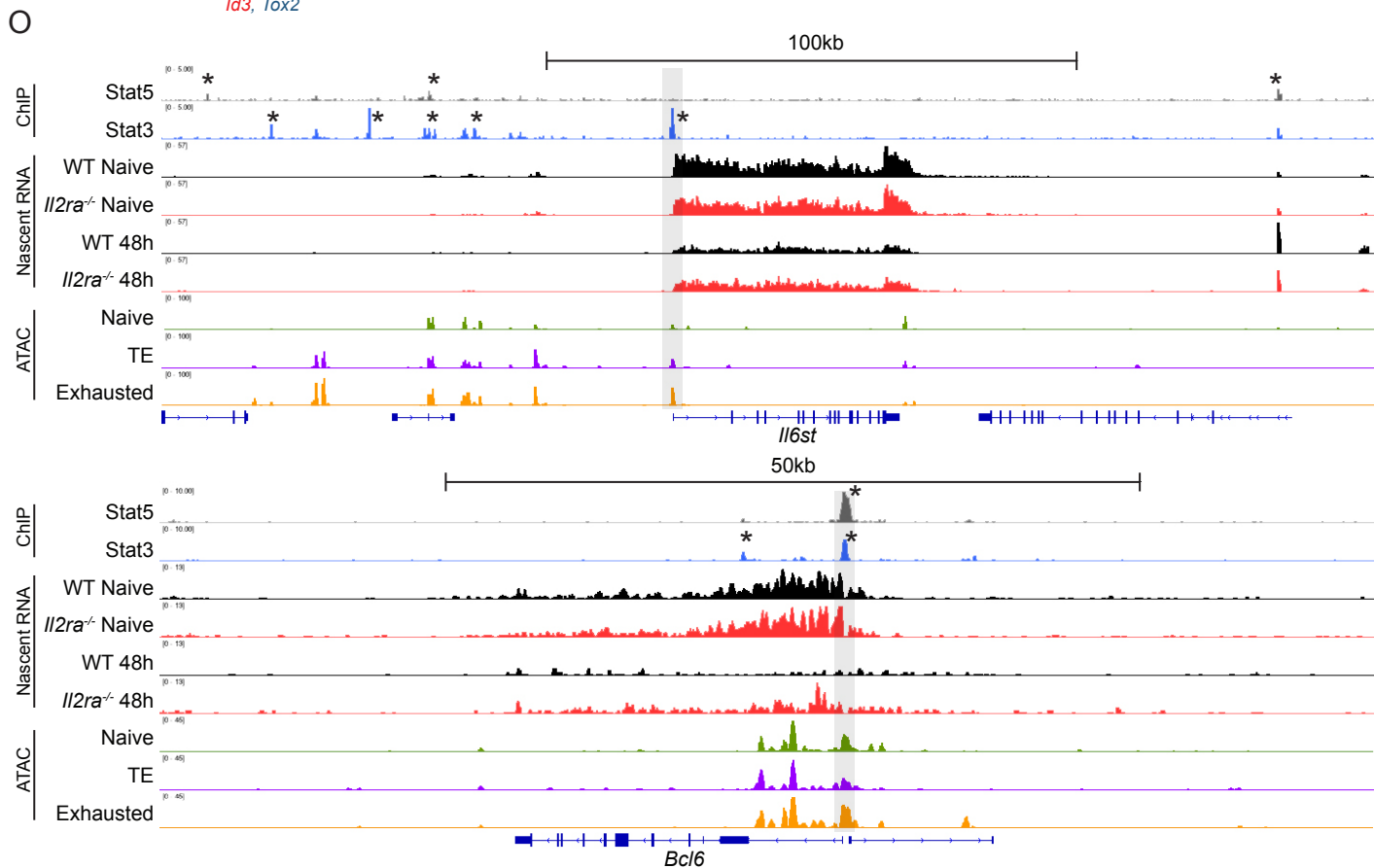
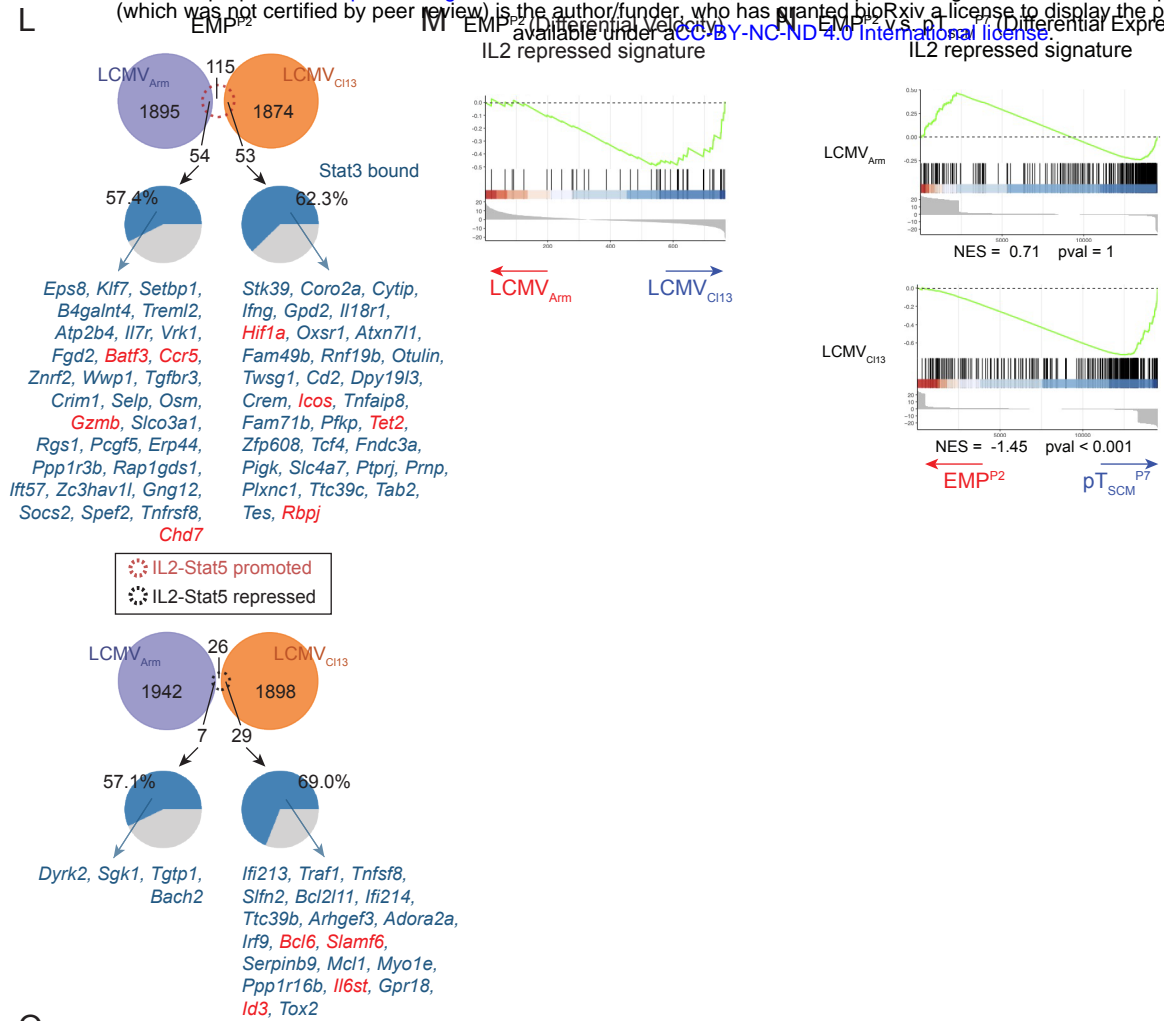
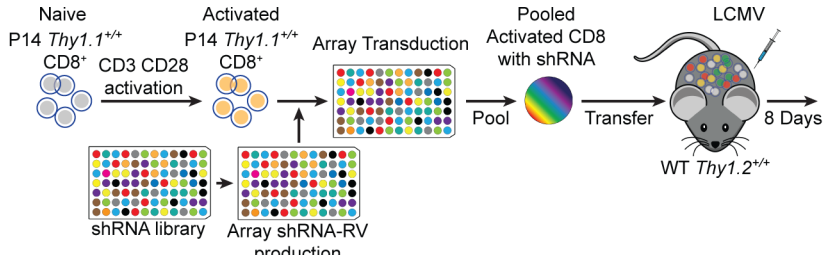


Figure S3

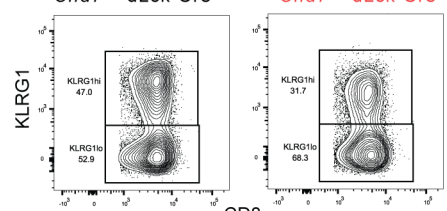
A RNAi screen experimental scheme



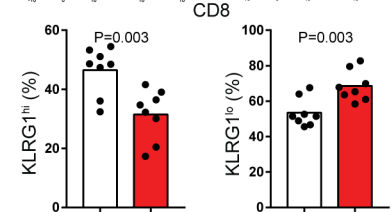
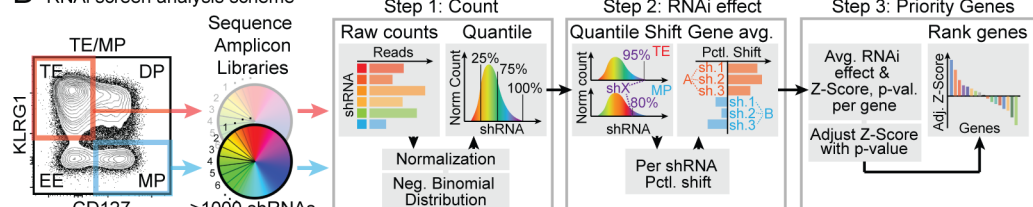
Gated splenic CD44^{hi} YFP+ GP33+ CD8+, 5 days p.i.

Chd7^{+/+} dLck-Cre

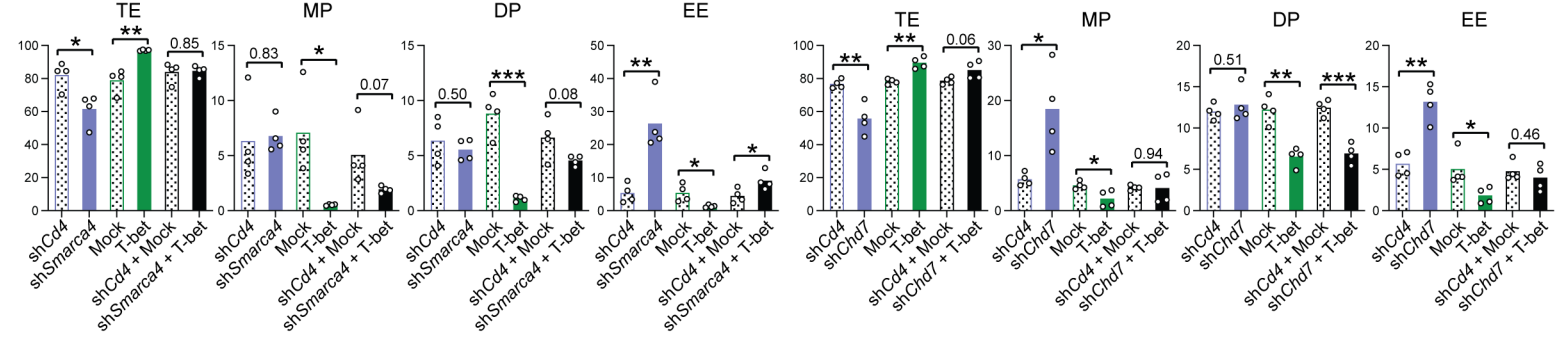
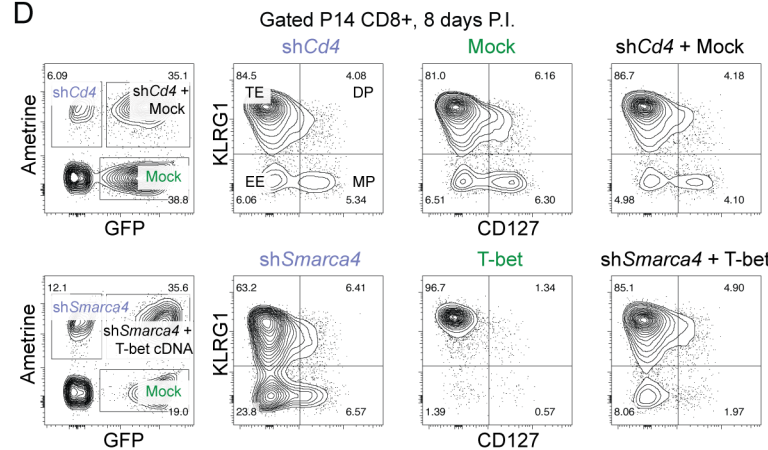
Chd7^{fl/fl} dLck-Cre



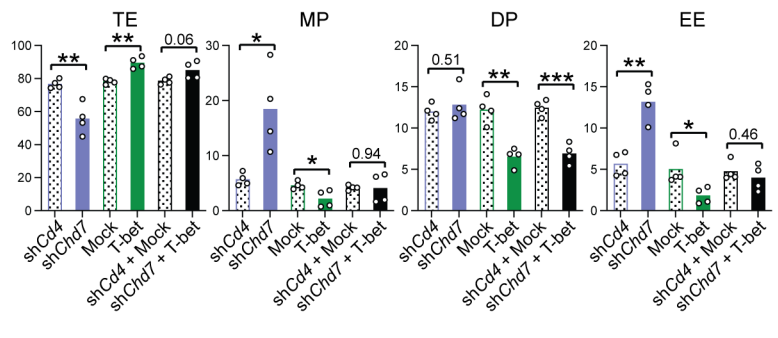
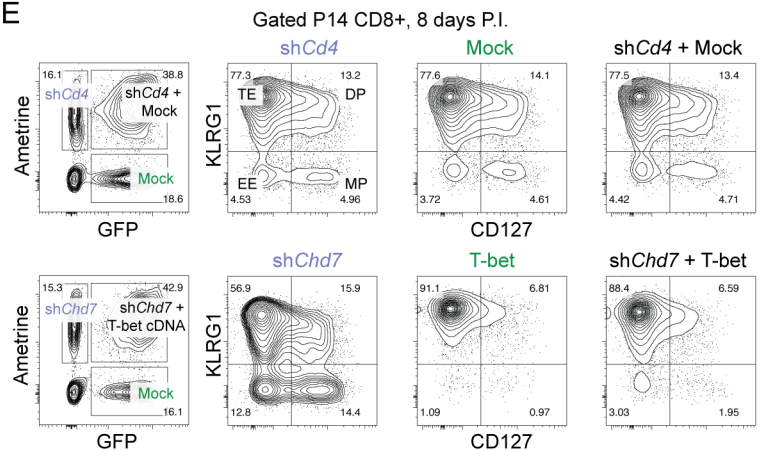
B RNAi screen analysis scheme



D



E



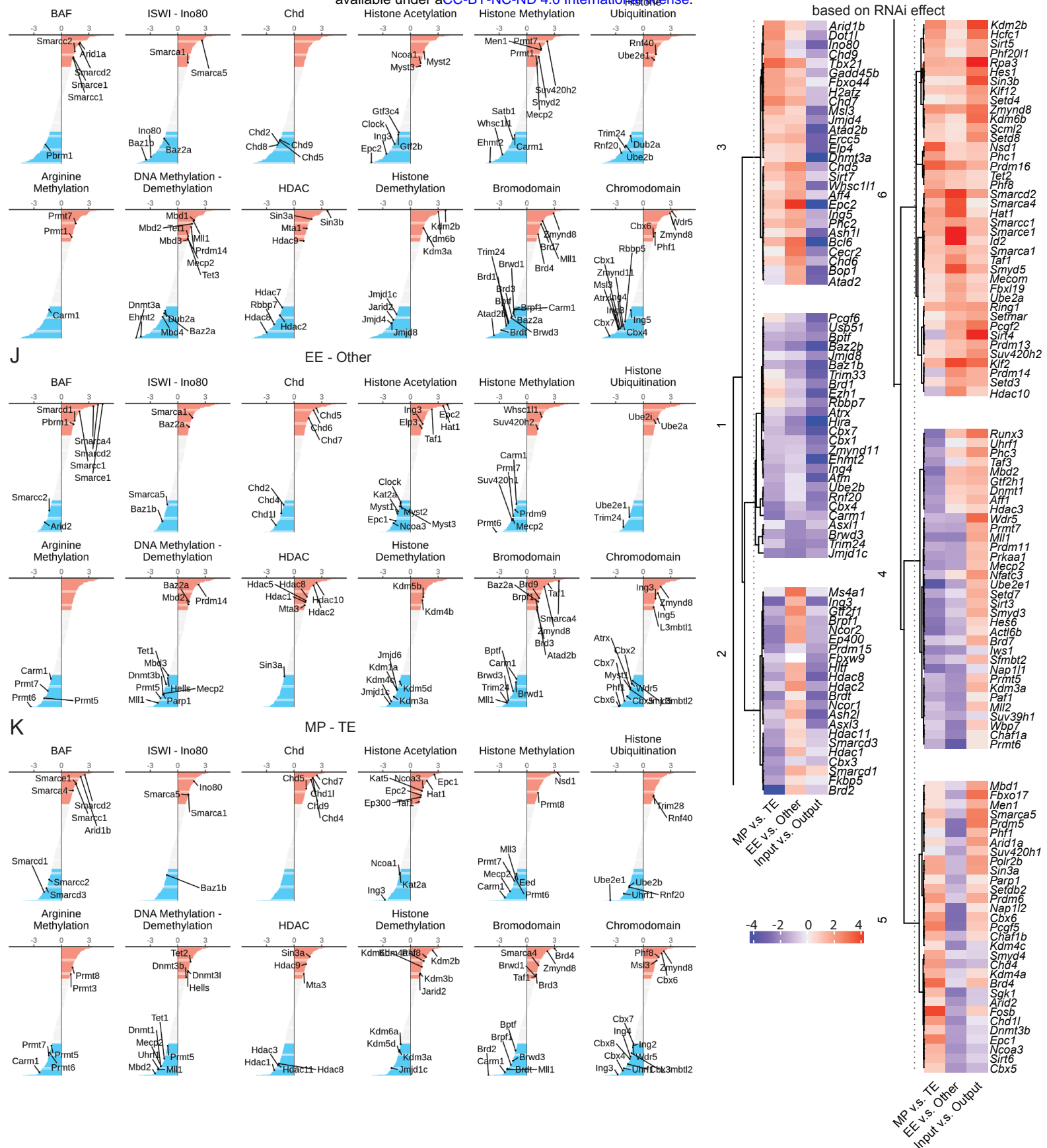
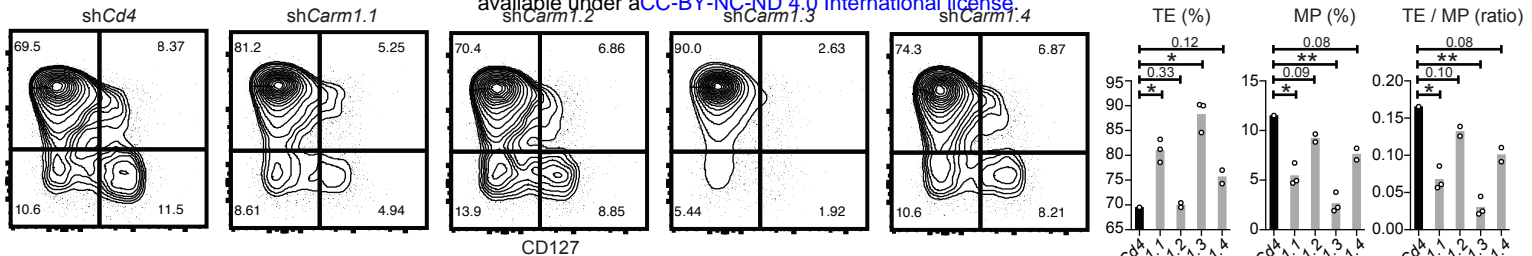
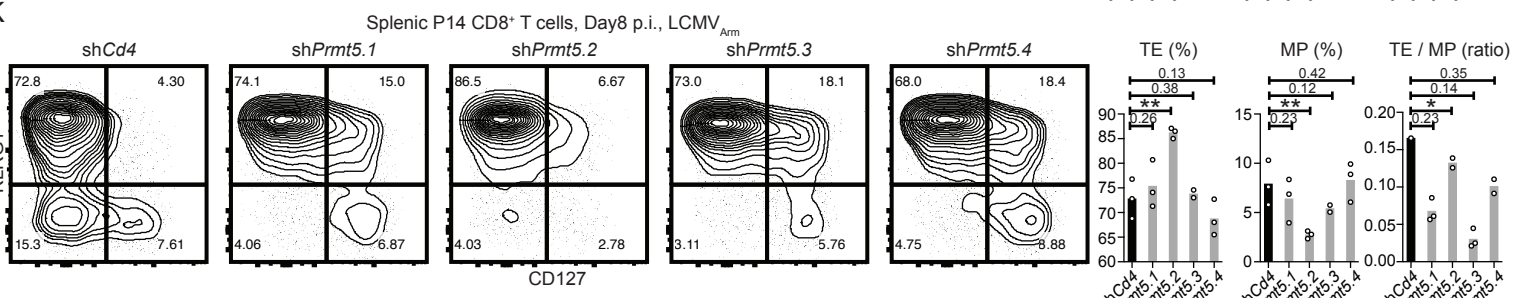


Figure S4

J



K



L

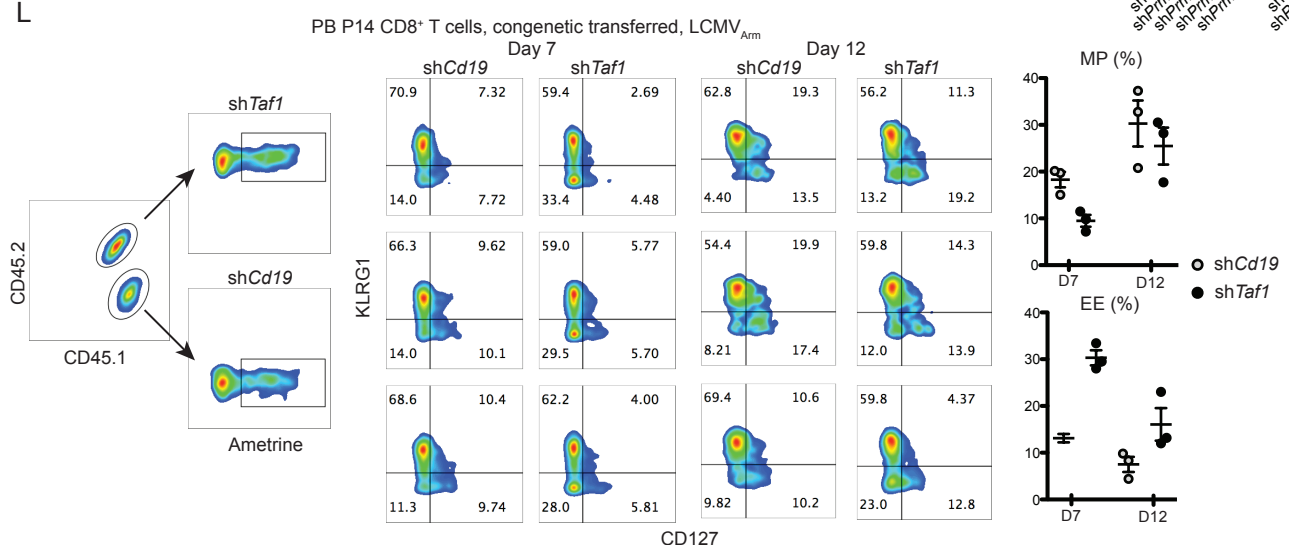


Figure S4